

1 Neuron-specific protein network mapping of autism risk genes identifies shared 2 biological mechanisms and disease relevant pathologies

3 *Nadeem Murtaza*^{1,2}, *Annie A. Cheng*², *Chad O. Brown*^{1,2}, *Durga Praveen Meka*³, *Shuai*
4 *Hong*³, *Jarryll A. Uy*^{2,4}, *Joelle El-Hajjar*¹, *Neta Pipko*¹, *Brianna K. Unda*², *Birgit*
5 *Schwanke*³, *Sansi Xing*¹, *Bhooma Thiruvahindrapuram*⁵, *Worrawat Engchuan*⁵, *Brett*
6 *Trost*⁵, *Eric Deneault*⁶, *Froylan Calderon de Anda*³, *Bradley W. Doble*⁷, *James Ellis*^{5,8},
7 *Evdokia Anagnostou*^{9,10}, *Gary D. Bader*⁸, *Stephen W. Scherer*^{5,8}, *Yu Lu*¹, *Karun K.*
8 *Singh*^{2,4*}

9
10 ¹Department of Biochemistry and Biomedical Sciences, Faculty of Health Sciences, McMaster University,
11 Hamilton, ON, Canada

12 ²Krembil Research Institute, University Health Network, Toronto, ON, Canada

13 ³Center for Molecular Neurobiology Hamburg (ZMNH), Research Group Neuronal Development,
14 University Medical Center Hamburg-Eppendorf (UKE), Hamburg, Germany

15 ⁴Department of Laboratory Medicine and Pathobiology, Faculty of Medicine, University of Toronto,
16 Toronto, ON, Canada

17 ⁵The Centre for Applied Genomics, The Hospital for Sick Children, Toronto, ON, Canada

18 ⁶Centre for Biologics Evaluation, Biologic and Radiopharmaceutical Drugs Directorate, Health Products
19 and Food Branch, Health Canada, Ottawa, Ontario, Canada

20 ⁷Department of Paediatrics, Department of Biochemistry and Medical Genetics, University of Manitoba,
21 Winnipeg, MB, Canada

22 ⁸Department of Molecular Genetics, Faculty of Medicine, University of Toronto, Toronto, ON, Canada

23 ⁹Department of Neurology, The Hospital for Sick Children, Toronto, ON, Canada.

24 ¹⁰Bloorview Research Institute, Holland Bloorview Kids Rehabilitation Hospital, Toronto, ON, Canada.

25

26 ***Correspondence:** karun.singh@uhnresearch.ca

27

28 Main Highlights:

- 29 1. Neuron-specific protein interaction screening of 41 ASD-risk genes to identify
30 new disease mechanisms at the protein level
- 31 2. High connectivity between multiple unrelated ASD-risk genes at the protein
32 interaction level
- 33 3. PPI networks show disease-relevant pathways including synaptic transmission,
34 metabolic pathways, Wnt signaling, ion channel activity, MAPK signaling
- 35 4. Metabolic pathways, such as TCA cycle and pyruvate metabolism, are altered in
36 neurons by multiple ASD-risk genes not previously linked to this pathway
- 37 5. Novel localization of uncharacterized ASD-risk gene PPP2R5D at the
38 synapse, which is disrupted by *de novo* mutations identified in patients
- 39 6. Clustering of ASD-risk genes based on PPI connectivity identifies multiple gene
40 groups that show correlation between mutation-type and clinical behavior scores,
41 revealing the importance of understanding PPI networks in ASD

42

43

44

45 **Abstract**

46 Autism spectrum disorder (ASD) is a genetically heterogeneous disorder.
47 Sequencing studies have identified hundreds of risk genes for autism spectrum disorder
48 (ASD), but the signaling networks of genes at the protein level remain largely
49 unexplored, which can provide insight into previously unknown individual and
50 convergent disease pathways in the brain. To address this gap, we used neuron-
51 specific proximity-labeling proteomics (BioID) to identify protein-protein interaction (PPI)
52 networks of 41 ASD-risk genes. Network analysis revealed the combined 41 risk gene
53 PPI network map had more shared connectivity between unrelated ASD-risk genes than
54 represented in existing public databases. We identified common pathways between
55 established and uncharacterized risk genes, including synaptic transmission,
56 mitochondrial/metabolic processes, Wnt signaling pathways, ion channel activity and
57 MAPK signaling. Investigation of the mitochondrial and metabolic network using gene
58 knockouts revealed a functional hub in neurons for multiple risk genes not previously
59 associated with this pathway. Further, we identified that the uncharacterized ASD-risk
60 gene PPP2R5D localizes to the synapse, which is disrupted by patient *de novo*
61 missense mutations. Investigation of *de novo* missense variants of additional synaptic
62 ASD-risk genes demonstrated that changes in PPI networks can capture synaptic
63 transmission deficits. The neuronal 41 ASD-risk gene PPI network map also revealed
64 enrichment for an additional 112 ASD-risk genes and human brain cell types implicated
65 in ASD pathology. Interestingly, clustering of ASD-risk genes based on their PPI
66 network connectivity identified multiple gene groups that correlate mutation-type to
67 clinical behavior scores. Together, our data reveal that using PPI networks to map ASD
68 risk genes can identify previously unknown individual and convergent neuronal signaling
69 networks, provide a method to assess the impact of patient variants, and reveal new
70 biological insight into disease mechanisms.

71

72

73

74

75

76

77

78

79

80

81 **Introduction**

82 Autism spectrum disorders (ASD) are a heterogeneous group of
83 neurodevelopmental conditions that manifest early in life, occurring in 1 in 66 children
84 under the age of 8¹. The risk of developing ASD has a strong genetic basis, including
85 common and rare genetic risk variants²⁻⁵. As such, numerous large scale whole exome
86 and genome sequencing studies have identified hundreds of genes associated with
87 ASD risk^{6,7,16,8-15}. While the mechanisms by which different risk genes lead to disease
88 are poorly understood, one hypothesis is that they converge functionally within brain
89 signaling networks. Understanding signaling convergence can help reveal the risk
90 genes that work through common pathways and have functional relationships. In turn,
91 this could help classify autism risk genes based on biological pathways, prioritize the
92 discovery of new risk genes, and identify convergent pathways that could be harnessed
93 for targeted therapy development.

94 The majority of convergent ASD-associated pathways discovered to date are
95 based on exome and genome sequencing, transcriptomics, and gene co-expression
96 analyses, including CRISPR/Cas9 knockout screens combined with single cell RNA
97 sequencing^{11,12,15,17-22}. These studies have implicated pathways such as synaptic
98 transmission, translation, transcription, chromatin remodeling and splicing^{19,23-26}.
99 However, the majority of autism risk genes encode proteins, and protein-protein
100 interactions (PPIs) are an essential mechanism of signaling^{8,9}. Therefore, non-protein
101 interaction-based networks, while important, lack information regarding which ASD-risk
102 genes interact with each other or converge into common signaling networks at the
103 protein level. Given that a large proportion of ASD genes have non-nuclear and non-
104 gene expression regulating functions^{15,27}, assessment of PPIs provides an unbiased
105 approach to gain insights into unknown convergent ASD disease processes^{28,29}.
106 Previous ASD sequencing studies have shown that that risk genes are part of core PPI
107 networks^{8,23,26,30}, and large yeast-two-hybrid (Y2H) studies have identified PPI networks
108 shared between ASD-risk genes^{31,32}. However, these data are extracted from
109 databases that are largely derived from non-neuronal cell lines and tissues, and do not
110 represent brain-specific networks³³. The lack of ASD risk-gene PPI networks in disease-
111 relevant cell types represents a missing link towards understanding the biological
112 mechanisms of ASD.

113 Multiple techniques can be used to identify PPIs, including affinity purification or
114 proximity-labeling proteomics combined with mass spectrometry (reviewed in Richards
115 *et al.*, 2021³⁴). Both are powerful approaches to identify PPI networks in cells but have
116 caveats that can be mitigated by using appropriate controls and validations. Further,
117 many brain-expressed genes are large in size, including ASD-risk genes³⁵, which limits
118 the systems that can be used for expression in cells and allow identification of their PPI
119 networks. We took an approach that balances gene size limitations, while at the same

120 time captures strong and transient interactions to build comprehensive PPI networks for
121 ASD risk genes. We developed a lentiviral *in vitro* proximity-labeling proteomics
122 (BioID2) system that uses mouse primary neurons. Proximity-labeling proteomics has
123 been used successfully to capture physiologically relevant interactomes in neural cell-
124 types both *in vitro* and *in vivo*^{36–39} or to map cellular compartments^{40–42}. Given the
125 implication of cortical neurons in ASD pathology^{25,43}, we captured PPI networks from
126 cortical neurons, while allowing them to grow with their glial counterparts to promote
127 proper maturation^{44–46}.

128 In the current study, we address the lack of brain cell type-specific PPI networks
129 for ASD-risk genes. We designed a screen to identify the interactome of 41 ASD-risk
130 proteins in neurons by using proximity-dependent biotinylation paired with mass
131 spectrometry. We targeted non-nuclear proteins (e.g., cytosolic proteins, receptors,
132 kinases, scaffold proteins, and intracellular signaling proteins) because nuclear proteins
133 have a high level of endogenous biotinylation and categorically different functional
134 pathways. Our screen found 1770 protein-level connections (direct and indirect)
135 between the 41 genes in neurons, which was approximately 20-times that reported in
136 the STRING database (at lowest confidence)⁴⁷. Convergent protein networks included
137 synaptic transmission, mitochondrial/metabolic processes and Wnt signaling. Further
138 investigation of genes not previously linked to mitochondrial/metabolic processes,
139 through gene-knockout approaches, revealed that multiple genes regulate mitochondrial
140 cellular respiration in mouse and human neurons. To further demonstrate the value of
141 applying PPI networks to study autism risk genes, we examined rare and *de novo*
142 missense variants in synaptic or poorly characterized ASD-risk genes. We found
143 disruption of key PPIs that led to functional deficits in synaptic transmission. Our PPI
144 network in mouse cortical neurons was cross-referenced with human data to
145 demonstrate its relevance to ASD pathology. Comparing the shared 41 ASD-risk gene
146 PPI network map to human sequencing data revealed an enrichment of an additional
147 112 ASD risk genes and expression in human brain cell types associated with ASD
148 pathology^{11–15}. More importantly, comparing the PPI network to human clinical data from
149 the MSSNG database (genome sequencing and clinical data from over 5,000
150 individuals with ASD)^{12,48}, we found that individuals with variants in risk genes with a
151 high degree of shared interactions have similar adaptive behavior scores.

152 Taken together, we demonstrate that neuron-specific PPI networks provide a
153 powerful approach to reveal novel individual and convergent disease mechanisms in
154 ASD. Given the scalability of our method and its underutilization in ASD research, we
155 believe our PPI network resource and screening system can be applied more broadly to
156 additional autism risk genes to identify previously unknown or overlooked disease
157 mechanisms that are not captured with current approaches.

158

159 **Main**

160 ***Development of a neuronal proximity-based proteomic system to identify PPI***
161 ***networks***

162 To identify the PPI networks of 41 ASD-risk genes, we used mixed mouse
163 cortical neurons and glia co-cultures infected with lentiviral constructs expressing
164 BioID2 fusion proteins (pLV-hSyn-tGFP-P2A-POI-13xLinker-BioID2-3xFLAG) (Extended
165 Fig. 1a). Neuron-specific expression of BioID2-tagged proteins was driven by a human
166 Synapsin1 promoter, and neuron/glia co-cultures were used to promote synaptic
167 maturation. A 13x Gly-Ser linker sequence was used to join proteins-of-interest (POIs)
168 with the BioID2-3xFLAG, which increases the range of biotinylation around the fusion
169 protein. To help monitor transduction efficiencies, TurboGFP (tGFP) was coexpressed
170 with BioID2 fusion proteins in a bicistronic system employing a P2A “self-cleaving”
171 peptide. We used a Luciferase-P2A-BioID2-3xFLAG construct as a negative control
172 (Extended Fig. 1b). Since lentiviral (LV) systems can accommodate larger gene sizes
173 than adeno-associated virus (AAV), we were able to perform BioID2 on larger proteins
174 such as SHANK3, GRIN2B, MET, SYNGAP1 and CNTNAP2.

175 Embryonic age 16-17 (E16-17) mouse pup cortices were harvested and cultured
176 until days in vitro (DIV) 14, then infected with the BioID2 fusion constructs by using a
177 lentivirus at an MOI of 0.7 (Fig. 1a). Biotin was added on DIV17 and cells were lysed
178 after 18 hours on DIV18 to allow maximal biotinylation time. To reduce variability
179 between mass spectrometry runs, TMT10plex isobaric-labeling was used to combine at
180 least 3 biological replicates per gene. One additional technical TMT-labeling replicate of
181 luciferase control sample chosen at random was used to account for differences in
182 labeling. Two statistical cut-offs were used to identify positive hits for the PPI networks
183 of each POI: Biotinylated proteins in the POI sample with 1) a significant increase in
184 Log₂ abundance compared to the luciferase control (Student’s t-test, $p < 0.05$)³⁶ and 2)
185 that were significant outliers when accounting for the overall protein abundance
186 compared to the protein abundance ratio between the POI and control samples (SigB
187 $p < 0.05$)⁴⁹. Protein abundances were normalized between biological replicates based on
188 the sample with the highest total protein abundance. To reduce variability between each
189 viral transduction, flow cytometry was used to determine the total abundance of GFP in
190 the infected neurons between samples. The abundance levels of samples that had less
191 total GFP (area under the curve in GFP intensity histogram) than the luciferase control
192 were normalized by the factor needed to minimally equal the luciferase control GFP
193 levels. To account for false positive hits due to variability in TMT-labeling between
194 samples, the ratio of protein abundances between the luciferase control technical TMT-
195 labeling replicates were used as the minimal required ratio between POI and control
196 sample abundances. Proteins that did not have abundance ratios (POI/Luciferase
197 control) higher than this minimal ratio were considered false positives and removed from

198 further analysis. Further, to promote high efficiency infections, we created an optimized
199 lentiviral production protocol to produce high-titer virus for small and large risk genes
200 (Fig. 1a). This BioID2 screen was used in five specific experimental outputs: to identify
201 1) shared molecular pathways, 2) the impact of patient genetic variants on the PPI
202 network, 3) correlation between ASD-risk genes, 4) enrichment of ASD-relevant cell
203 types in the shared PPI network map, and 5) correlation of clinical phenotypes with the
204 ASD-risk genes (Fig. 1a).

205 To validate the BioID2 screening system, we used the well characterized
206 excitatory synapse protein DLG4 (PSD95). Neurons expressing PSD95-BioID2
207 displayed punctate localization of BioID2-3xFLAG fusion proteins and biotinylated
208 proteins around the dendrites, suggesting appropriate synaptic expression and
209 biotinylation (Extended Fig. 1c). The Luciferase-P2A-BioID2 control showed non-
210 specific localization and biotinylation throughout the neuron, which is expected
211 (Extended Fig. 1c). We identified 74 proteins that interact with PSD95, and Reactome
212 pathway enrichment revealed neurotransmitter receptors and glutamatergic synapses,
213 as expected (Extended Fig. 1d and Supplementary Table 1). Enriched pathways also
214 include less directly associated networks, such as GABAergic synapses, Rho GTPase
215 signaling, and Wnt signaling. Comparison of our PSD95 PPI network with the previously
216 published PPI networks for PSD95, from *in vivo* mouse BioID and *in vivo* mouse tandem
217 affinity purification^{36,50}, revealed 25 shared proteins between all three datasets
218 (Extended Fig. 1e), highlighting that our BioID2 system captures relevant networks. The
219 distinct and partially-shared proteins from the other systems suggest differences
220 between proximity-labeling and affinity purification methods and/or *in vitro* and *in vivo*
221 approaches.

222 Cortical neurons are a major cell type associated with ASD¹⁵; however, scalable
223 BioID labeling approaches have been done primarily in cell lines, such as HEK293
224 cells⁴⁰. To determine the necessity and importance of using neurons for the BioID2
225 screen of ASD-risk genes, we performed BioID2 in HEK293 cells using PSD95, and a
226 subset of ASD risk genes including *ETFB*, *SPAST*, *STXBP1*, *SYNGAP1*, and *TAOK2*
227 (Extended Fig. 2 and Supplementary Table 2). The PSD95 PPI network from HEK293
228 cells showed enrichment of many pathways, including EGF- and NTR-receptor signaling
229 and cell junction organization, but there was a complete absence of synaptic pathways
230 (Extended Fig. 2a). Furthermore, BioID2 of all six ASD risk proteins in HEK293 cells
231 revealed a significant loss of protein interactions localized in neuron-specific
232 compartments, and large differences in the PPI network between HEK293 cells
233 compared to mouse neurons (Extended Fig. 2b-g and Supplementary Table 3). While
234 HEK293 cells yield interaction networks for ASD risk genes, they may not have
235 relevance to pathways associated with brain-specific pathophysiology of
236 neurodevelopmental disorders.

237 To further validate the specificity of our neuron-specific BioID2 screening system,
238 we targeted proteins associated with compartments⁵¹, including microtubules (MAP2C),
239 the endoplasmic reticulum network (CANX), plasma membrane (PDGFR
240 transmembrane domain), trans-Golgi apparatus (TGOLN), the presynaptic terminal
241 (SNCA), and the nuclei (MECP2). Cellular compartment analysis of each PPI network
242 revealed enrichment of the compartments expected for MAP2C, MECP2, CANX,
243 PDGFR-TM domain, and TGOLN (Extended Fig. 3, Extended Fig. 4d and
244 Supplementary Table 1 and 4). SNCA did not have a strong enrichment of presynaptic
245 compartments; however, it did identify enriched pathways involving axons, growth
246 cones and the synapse (Extended Fig. 3e). BioID2 of MECP2, a nuclear protein,
247 indicated localization to the nucleus (Extended Fig. 4a) and interaction with proteins
248 enriched in nucleus-specific pathways, such as transcription regulation and mRNA
249 splicing (Extended Fig. 4b). The MECP2 PPI network in mouse neurons had differences
250 in protein interactions compared to the MECP2 network in HEK293 cells, but there was
251 no enrichment for neuron-specific compartments (Extended Fig. 4c, d). The difference
252 in identified proteins suggests that mouse neurons have differing MECP2 interactions
253 that are localized to the nucleus. Further, the PPI network of MECP2 did not include
254 some of the known protein interactions in mouse neurons (e.g., ATRX, CREB1, SIN3A,
255 NCor, and TET1), suggesting that our system may not be optimized for nuclear
256 proteins, possibly due to the presence of highly biotinylated endogenous proteins. The
257 enrichment of proteins specific to each compartment provides additional validation that
258 the BioID2 screen in mouse cortical neurons can provide relevant PPI networks.

259 ***Identification of a shared PPI network map and common pathways of 41 ASD-risk*** 260 ***genes***

261 To develop a shared PPI network map for ASD risk genes, we selected 41 ASD-
262 risk genes that encode proteins with a range of molecular functions, including regulation
263 of phosphorylation and ubiquitination, enzymatic control of metabolism, protein
264 regulation and transport, and synapse formation and function (Fig. 1b). These genes
265 were chosen from a combined list of ASD-risk genes from the SPARK, SFARI category
266 1, 2, and syndromic gene lists and previous sequencing studies^{11–16}. For each gene, the
267 human cDNA was cloned into a BioID2 lentiviral backbone and protein expression was
268 confirmed with western blotting (Extended Fig. 5). All BioID2 fusion constructs were
269 found to be the expected size through western blotting; however, some constructs
270 showed a second larger size protein due to lower P2A efficiency or increased cleaved
271 BioID2-FLAG (lowest band) due to increased degradation (Extended Fig. 5). As
272 mentioned previously, the list includes large genes (>4kb) such as SHANK3 and
273 SYNGAP1, allowing us to examine the PPI network of proteins from a range of sizes. All
274 genes that were chosen for the screen have cytoplasmic functions. Nuclear genes were
275 not selected because it has previously been shown there is a separation in function

276 between nuclear gene regulating proteins and cytoplasmic neural communication
277 proteins¹⁵. We identified the individual PPI networks and enriched Reactome pathways,
278 biological processes and cellular compartments for each of the 41 ASD-risk genes.
279 These data can be found in Supplementary Table 1 and Supplementary Table 5, and
280 are meant to be a resource for the research community.

281 The 41 ASD-risk gene PPI network consisted of 1109 proteins (41 ASD bait
282 proteins and 1068 prey proteins) and 2349 connections. Half of the identified prey
283 proteins were shared between 2-15 ASD bait proteins (489 prey proteins and 1770
284 connections), and of these, 15 prey proteins were shared between at least 10 different
285 ASD bait proteins. Every ASD bait protein shared at least 4 interactions (direct or
286 shared prey protein) with one other ASD bait protein, with up to 38 shared interactions
287 between DLG4 and SYNGAP1 (Fig. 2a). The PPI network of 31 out of the 41 ASD bait
288 genes showed direct interaction with at least 1 other ASD bait protein. Reciprocal
289 identification was observed between DLG4 and CDKL5, SYNGAP1, GRIA1, or GRIA2
290 and between GRIA1 and GRIA2. The most identified ASD bait proteins were GRIN2B,
291 PPP1R9B, GRIA2, and KCNQ2. Conversely, BioID2 of TAOK2, CDKL5, DLG4,
292 LRRC4C, and SYNGAP1 identified the most ASD bait proteins, suggesting high
293 connectivity between a subset of ASD bait proteins. To determine the utility of creating
294 an ASD PPI network in neurons, we compared our results with physical interactions
295 between the 41 ASD bait genes extracted from the STRING database (greater than or
296 equal to medium confidence, 0.4). Our BioID2 ASD-risk gene PPI network had 245
297 connections (where each connection represents at least 5 shared protein interactions)
298 between 36 of the 41 ASD bait proteins. The STRING database had 33 direct
299 interactions between 23 of the bait proteins, revealing a near 50-fold increase in the
300 number of connections within our ASD-risk gene PPI network (Fig. 2a, b). Current
301 databases, such as STRING, are primarily derived from non-neuronal sources using
302 gene co-expression or direct interaction data³³. However, our PPIs were identified in
303 neuronal cells and include both direct interacting proteins and shared interacting
304 proteins that highlight important connections missed by traditional methods.

305 The most significant pathways in the shared 41 ASD-risk gene PPI network
306 involve synaptic transmission, demonstrating that our system can identify the most
307 frequently identified pathways in ASD pathophysiology (Fig. 2c and Supplementary
308 Table 6). Other enriched pathways included TCA cycle and mitochondrial activity, Wnt
309 signaling, potassium channel activity, and MAPK signaling (Fig. 2c and Extended Fig.
310 6a). These enriched pathways suggest that synaptic function plays a core role among
311 non-nuclear ASD risk proteins, but it is not the only pathway involved between the 41
312 genes. The majority of the shared ASD-risk PPI network localized to specific cellular
313 compartments including axons, dendrites and synapses (Extended Fig. 6b and
314 Supplementary Table 6), while the majority of biological processes involve synaptic

315 signaling and organization, and protein transport (Extended Fig. 6c and Supplementary
316 Table 6). Shared pathways in the ASD-risk gene PPI network reflect the major role of
317 synaptic dysfunction in ASD, but also highlight that other, less well-studied pathways
318 are important contributors to convergent ASD pathology.

319 ***The shared PPI network map identifies the tricarboxylic acid (TCA) cycle and***
320 ***pyruvate metabolism as a common signaling pathway in ASD***

321 One rationale for constructing a PPI network map with ASD-risk genes was to
322 identify novel or poorly characterized convergent signaling mechanisms. In this regard,
323 one of the top pathways we identified was the TCA cycle and pyruvate metabolism
324 (mitochondrial/metabolic processes), implicating dysregulation in mitochondrial function
325 and cellular metabolism. This pathway has been associated with a few ASD associated
326 genes^{52–54}, but the mechanisms are not well understood, and it is unknown whether
327 other ASD risk genes regulate mitochondrial/metabolic processes. Interestingly,
328 previous ASD clinical studies have identified abnormal mitochondrial function in patient
329 lymphoblastoid cells^{55–58}, but whether this occurs in mammalian brain cells is unknown.
330 TCA cycle and pyruvate metabolism proteins were highly enriched in the shared ASD-
331 risk gene PPI network map (adj. p-value = 3.14×10^{-12}), even without the PPI network for
332 the mitochondrial protein ETFB (adj. p-value = 1.35×10^{-7}) (Supplementary Table 6). 28
333 out of 41 ASD-risk genes were found to be interacting with at least one TCA cycle and
334 pyruvate metabolism associated protein (Fig. 3a). Citrate synthase (CS), which is
335 involved in turning acetyl-CoA into citrate early in the TCA cycle, was found to interact
336 with eight ASD bait proteins (ERBIN, MET, NRXN1, SHANK3, SPAST, STXBP1,
337 SYNGAP1, TAOK2). The TCA cycle and pyruvate metabolism are essential for proper
338 cellular respiration. Therefore, we investigated this finding by focusing on a gene in our
339 screen that was not previously associated with mitochondrial and metabolic processes
340 in the brain, *TAOK2*, a gene in the 16p11.2 deletion/duplication region associated with
341 ASD^{59–62}. We measured cellular respiration using live-cell metabolic assays in a *Taok2*
342 knockout (KO) mouse model, which we previously demonstrated has deficits in synapse
343 formation and function⁵⁹. *Taok2* heterozygous knockout (Het) cultured mouse cortical
344 neurons showed a significant increase in maximal respiration, proton leak, non-
345 mitochondrial respiration, and spare respiratory capacity, and a decrease in ATP
346 coupling efficiency (Fig. 3b, c and Extended Fig. 7a-d) compared to wildtype (WT)
347 neurons. These changes suggested the presence of less functional mitochondria, which
348 was corroborated by proteomic analysis of post-synaptic density fractions isolated from
349 *Taok2* WT and KO mouse cortices (Extended Fig. 7e). *Taok2* KO mice PSD fractions
350 had significant downregulation of proteins involved in synaptic function and activity, and
351 also in respiratory ETC complex proteins (Extended Fig. 7f and Supplementary Table
352 7). Analysis at the transcriptome level also revealed reduced mRNA levels of
353 mitochondrial membrane proteins in *Taok2* KO mouse cortices (Extended Fig. 7g, h and

354 Supplementary Table 7), coinciding with the reduced protein levels of mitochondrial
355 proteins (Extended Fig. 7e, f). Further investigation revealed that *Taok2* Het and KO
356 neurons have a reduced proportion of active TMRM stained mitochondria (Fig. 3d, e
357 and Extended Fig. 7i), and an overall increase in the amount or size of mitochondria
358 labeled by TOMM20, an outer membrane protein (Fig. 3f, g). These data implicate
359 dysregulated mitochondria in the absence of *Taok2*; therefore, we examined the
360 morphology of mitochondria *in vivo* from electron microscopy (EM) images taken from
361 WT and *Taok2* KO mouse cortical excitatory neurons⁵⁹. We found that *Taok2* KO
362 mouse neurons had altered mitochondrial morphology with a reduction in category 1
363 and 3 mitochondria, which show more typical mitochondria morphology, and an
364 increase in category 2 mitochondria at their synapses (Fig. 3h, i)⁶³. Category 2
365 mitochondria have enlarged non-contiguous mitochondrial cristae⁶³, which can cause
366 reduced oxidative phosphorylation and prevent proper translation and insertion of inner
367 membrane proteins^{64,65}. We extended our mouse studies to examine whether TAOK2
368 regulates mitochondrial/metabolic processes in human induced pluripotent stem cell
369 (iPSC)-derived NGN2-neurons. We used CRISPR/Cas9 to generate isogenic *TAOK2*
370 homozygous KO and heterozygous knock-in *TAOK2 A135P* iPSC lines. A135P is a *de*
371 *novo* missense variant which we previously demonstrated renders TAOK2 as kinase
372 dead⁵⁹. We generated human neurons through direct differentiation of iPSCs via NGN2
373 overexpression and found altered cellular respiration in *TAOK2* KO neurons (Extended
374 Fig. 7j) similar to mouse neurons, and significant increases in the spare respiratory
375 capacity of *TAOK2* KO and *A135P* neurons (Extended Fig. 7k). Human neurons
376 transfected with Mito7-DsRed also displayed an increase in mitochondrial puncta size in
377 *TAOK2* KO and *A135P* neurons, suggesting an increase in the number or size of the
378 mitochondria, similar to that observed in the mouse neurons (Extended Fig. 7l, m). To
379 determine if these changes were due to long-term developmental deficits caused by
380 loss of TAOK2 function, we used acute shRNA knock-down through *in utero*
381 electroporation and found that *Taok2* knock-down in cultured mouse neurons caused
382 decreased mitochondrial membrane potential (Extended Fig. 8a-c) similar to that
383 detected in the knockout mice (Fig. 3d, e). Taken together, using *TAOK2* as a validation
384 gene from the identified mitochondrial/metabolic PPI network, we determined that
385 mouse and human models with disruption of *TAOK2* have altered cellular respiration,
386 likely caused by altered activity, size and number of mitochondria.

387 To determine if other ASD risk genes converging on the mitochondrial/metabolic
388 network regulate cellular respiration, we used the CRISPR/Cas9 system to knock out
389 *Syngap1*, *Taok2*, and *Spast*. We also targeted *Etfb* and *Rheb*, which are both ASD risk
390 genes known to localize to the mitochondrion or regulate neuronal mitochondrial
391 function⁶⁶. Combined gRNAs against BFP and Luciferase were used as a negative
392 control^{67,68}, and we used 1-3 gRNAs targeting different genomic regions of the ASD-risk
393 genes (Extended Fig. 8d). Mouse cortical neurons were infected with Cas9-EGFP and

394 gRNA-mCherry lentiviral constructs. Western blots of neurons infected with Taok2
395 gRNAs and Cas9 showed decreased expression by approximately 50%, suggesting a
396 partial knockout (Extended Fig. 8e). CRISPR/Cas9 knockout of *Etfb*, a subunit of
397 riboflavin required for proper electron transfer in the ETC, showed increased basal and
398 maximal respiration, proton leakage, and no change in ATP synthase-dependent
399 cellular respiration (Fig. 3j, k and Extended Fig. 8f, g). These changes may correspond
400 to increased cellular respiration to counteract faulty ETC electron transfer. Mouse
401 neurons with CRISPR knockout of *Taok2*, *Syngap1*, and *Rheb* also showed significant
402 or trending changes in many aspects of cellular respiration (Fig. 3j, k and Extended Fig.
403 8f-i). CRISPR KO of *Spast* did not cause significant changes in cellular respiration,
404 possibly due to subtle effects or a role in different aspects of mitochondrial function. The
405 increase in basal respiration in *Taok2*, *Syngap1*, and *Etfb* KO neurons (Extended Fig.
406 8f) may be indicative of an acute effect, where altered cellular respiration has not yet
407 reached homeostasis within the neuron⁶⁹. These findings suggest that a subset of ASD
408 risk genes regulate cellular respiration in neurons, and highlight the relevance of TCA
409 cycle and pyruvate metabolism pathways in the developing brain as a risk factor for
410 ASD when dysregulated.

411 ***PPI networks identify differences in signaling between missense variants in ASD*** 412 ***risk genes***

413 Next, we hypothesized that PPI networks could be used to study missense
414 variants, which are a large and important class of genetic risk factors for ASD that have
415 less obvious functional impacts compared to loss-of-function (LoF) variants. Sequencing
416 of ASD individuals have identified many missense variants of unknown significance
417 (VUS) and therefore, the biological impact of variants in the majority of risk genes
418 remain unknown. Understanding the impact of a variant is important because it provides
419 the affected individual and family with a possible causal explanation and, in some
420 cases, it could help to assess clinical trajectory or treatments. Missense variants have
421 been suggested to impact protein stability and protein-protein interaction networks³⁰;
422 however, these data were imputed from databases using primarily non-neuronal
423 datasets, and were not tested in neurons. We used BiID2 to identify differences in
424 severity and pathogenic mechanisms of *de novo* missense variants identified in
425 individuals diagnosed with ASD. Due to the strong link between synaptic functional
426 deficits and ASD pathophysiology, we chose two known synaptic genes (TAOK2 β and
427 GRIA1) and a less well-characterized risk gene with no specific cellular localization
428 (PPP2R5D) (Fig. 4a-c, Supplementary Table 8, and Supplementary Table 9).

429 We used BiID2 to determine the change in the TAOK2 β PPI network due to the
430 A135P *de novo* missense variant, which was identified in an individual with ASD. The
431 TAOK2 β A135P PPI network had a reduced number of proteins associated with the

432 synaptic compartment, and simultaneously had increased dendritic and ribosomal
433 proteins (Fig. 4d). The latter changes may be due to the loss of PPI network proteins in
434 dendritic spines where TAOK2 β localizes, and an increase in dendritic and ribosome
435 translation complex protein interactions specific to the TAOK2 β A135P (Fig. 4e),
436 combined with the decreased expression of the A135P mutant (Extended Fig. 9a). To
437 corroborate the possible synaptic deficits caused by the A135P variant, we performed
438 patch-clamp electrophysiology on the isogenic iPSC-derived NGN2-neurons (Extended
439 Fig. 9b)⁷⁰⁻⁷². TAOK2 KO and TAOK2 A135P neurons had decreases in frequency and
440 amplitude of spontaneous excitatory post-synaptic currents (sEPSCs) (Fig. 4f, g),
441 corroborating the shift in interaction with synaptic proteins. The lack of change in the
442 intrinsic firing properties or Synapsin1-positive punctae density in TAOK2 A135P
443 neurons, as opposed to the TAOK2 KO neurons (Extended Fig. 9c-g), suggest that the
444 shift in interaction and localization for the heterozygous A135P line has dissimilar
445 phenotypes compared to the complete loss of TAOK2. In fact, TAOK2 A135P neurons
446 displayed increased size of Synapsin1 punctae, suggesting possible changes in the
447 synaptic structure (Extended Fig. 9c, d). Taken together, the TAOK2 β A135P variant
448 showed significant decreases in synaptic pathway protein interactions, demonstrating
449 that changes in PPI networks can be predictive of functional deficits.

450 We also asked whether PPI networks can distinguish the impact of missense
451 variants based on their location within functional domains of a gene. We investigated
452 GRIA1 and two *de novo* missense variants, R208H and A636T^{3,73,74}, located in the
453 extra-cellular ligand binding domain and the transmembrane domain, respectively (Fig.
454 4b). The GRIA1 variants showed strong differential effects in their enriched cellular
455 compartments (Fig. 4h) and the number of shared interacting proteins with the wildtype
456 (Fig. 4i). GRIA1 R208H had a significant loss of proteins localizing to the AMPA
457 receptor and post-synaptic density, which suggests functional changes in synapse
458 function. GRIA1 A636T had a less severe impact, with small increases in the number of
459 compartment-specific protein interactions and gains in membrane junction and ER
460 proteins (Fig. 4h and Supplementary Table 8 and 9), suggesting possible trafficking
461 issues. There were no changes in expression between the two variants (Extended Fig.
462 9h). To functionally corroborate the changes in PPI networks, we infected mouse
463 cortical neurons with the GRIA1 WT and both variants to obtain whole-cell voltage
464 clamp recordings. This revealed a trend towards decreased sEPSC frequency in
465 neurons expressing the R208H variant, but not the A636T variant (Fig. 4j, k). Although
466 the A636T mutant had no change in sEPSCs, we did observe large sEPSC bursts (Fig.
467 4j), which may be indicative of altered trafficking of AMPA receptors through the ER
468 network and longer turnover rates^{75,76}. Together, the stronger loss of interactions for
469 R208H compared to A636T coincide with the electrophysiology results, demonstrating
470 that BioID2 PPI networks can reveal functional differences in missense variants for
471 receptor proteins.

472 Finally, we used BioID2 to test missense variants in the risk gene PPP2R5D, a
473 regulatory subunit of phosphatase-2A⁷⁷. This protein is not known to have multiple
474 functional domains or a specific localization; therefore, BioID2 could help to first
475 understand where it functions in neurons and then the impact of ASD missense
476 variants. We selected three *de novo* PPP2R5D variants, P53S, E198K, and E420K,
477 which are spread throughout the protein^{77,78}. The PPI networks for the variants had both
478 common and dissimilar effects (Fig. 4c, l, and m), with all three variants reducing
479 interactions with synaptic and dendritic proteins enriched in the wildtype PPI network
480 (Fig. 4l). This suggests that PPP2R5D has a potential role in dendrites and synapses
481 based on PPI network. Additionally, all of the variants caused a loss and gain of diverse
482 interactions (Fig. 4m), with no change in expression levels (Extended Fig. 9i).
483 Interestingly, both the E198K and the E420K variants gained trans-Golgi compartment
484 proteins (Fig. 4l and Supplementary Table 8 and 9), suggesting altered localization.
485 Previous studies have described an overactive AKT pathway caused by the PPP2R5D
486 E420K variant⁷⁹. However, measurement of phospho-AKT levels in HEK293 cells
487 expressing the variants revealed no difference (Extended Fig. 9j), suggesting that
488 specific molecular assays may miss functional deficits. To probe E420K further, we
489 performed imaging on neurons and found accumulation of E420K in the cell body,
490 indicating possible trafficking deficits that cause increased interactions with trans-Golgi
491 network proteins (Fig. 3n). Together, the BioID2 approach revealed dendritic and
492 synaptic localization of PPP2R5D, which is lost in multiple missense variants that have
493 their own subtle differences. The differences in the PPI network of wildtype proteins and
494 their ASD-associated variants highlight the utility of the system to screen multiple
495 disease variants within a gene.

496 ***The 41 ASD-risk gene PPI network map enriches for additional ASD risk genes,***
497 ***human disease cell types, and correlates with human behavioral phenotypes from***
498 ***clinical datasets***

499 The complete PPI network map from the 41 ASD-risk genes demonstrates the
500 importance of a neuron-specific network. The network ultimately contained significantly
501 more connections than reported in databases such as STRING (Fig. 2a, b) and
502 elucidated multiple convergent pathways (e.g., TCA and pyruvate signaling, Fig. 2c)
503 linked to ASD that are poorly studied. To further demonstrate the utility of the 41 ASD-
504 risk gene PPI network map resource, we used enrichment analysis to determine
505 relevance to human ASD. We found a significant enrichment of 112 additional ASD-risk
506 genes (Fisher's Exact test $p = 2.69 \times 10^{-30}$, OR = 3.45), highlighting the strong functional
507 connectivity between ASD-risk genes at the protein level (Fig. 5a). Along with
508 enrichment of ASD-risk genes from the original 41 ASD-risk protein baits, we found that
509 gene lists reported from individual sequencing studies were enriched, especially when
510 examining cytoplasmic (non-nuclear) proteins (Extended Fig. 10a). This suggests strong

511 connectivity of ASD protein signaling outside the nucleus. Gene lists with only nuclear
512 proteins were not enriched (Extended Fig. 10b), providing evidence that there is less
513 interaction between proteins localized to the nucleus and those in the cytoplasm. Of the
514 153 ASD-risk proteins in the network, 69 are interacting with 2 or more ASD bait
515 proteins. *Slitrk5*, *Gria2*, *Dlg4*, *Grin2b*, and *Shank2* were identified by more than eight of
516 the ASD bait proteins, suggesting a potential central role for these genes in ASD
517 pathology. Enrichment of multiple cytoplasmic ASD-risk proteins in the PPI network
518 indicates functional connectivity between intracellular signaling proteins.

519 While the PPI network from 41 ASD-risk genes was generated using human
520 genes, it was obtained in a background of mouse cortical neuron and glia co-cultures;
521 therefore, it is unknown whether this network map is applicable to human brain cell
522 types or differentially expressed genes (DEGs) implicated in ASD pathology. To
523 address this, we examined the enrichment of specific cell types based on their single
524 cell RNA-sequencing profiles^{25,43}. We found that the 41 ASD-risk gene PPI network map
525 strongly enriches for excitatory and inhibitory neuron cell types, along with neural
526 progenitor cells, astrocytes and microglia (Fig. 5b), which have been associated with
527 ASD pathophysiology^{17,18,25,80,81}. When examining the ASD-specific DEGs of different
528 cell types from human post-mortem brain samples²⁵, the shared PPI network was
529 enriched for DEGs in layer 2/3 and 4 neurons, parvalbumin and VIP interneurons, and
530 protoplasmic astrocytes (Fig. 5c). The enrichment of ASD DEGs of specific cell types
531 highlights the human disease relevance of the 41 ASD-risk gene PPI network map.

532 Finally, we hypothesized a potential relationship between highly connected
533 genes within the 41 ASD-risk gene PPI network map and human ASD behavioral
534 phenotypes. This would link gene clusters to human phenotypes, and provide additional
535 insight into the biological basis of ASD. We took the individual PPI networks of the 41
536 ASD-risk genes and identified 3 groups (labeled Group 1, 2 and 3) of highly connected
537 ASD-risk genes, using the correlation between their individual PPI networks (Fig. 5d).
538 Groups 1 and 2 showed high connectivity between the ASD-risk genes within each
539 group, whereas connectivity was lower in Group 3. To determine if grouping the 41
540 ASD-risk genes is correlated with clinical ASD behavioral scores based on shared PPI
541 networks, we obtained clinical data of individuals with rare variants in the 41 ASD-risk
542 genes from the MSSNG database. The database contained the sequenced genomes of
543 a total of 4,258 families and 5,102 ASD-affected individuals at the time of data
544 extraction¹². We obtained the adaptive behavior and socialization scores from up to 879
545 individuals who possess at least one rare missense/splicing/LoF variant in the 41 ASD-
546 risk genes (data-explorer.mss.ng). Remarkably, we found that individuals with missense
547 variants in Group 1 genes had lower adaptive behavior standard scores compared to
548 Groups 2 or 3, suggesting that missense variants strongly impact the function of Group
549 1 genes in regards to adaptive behavior (Fig. 5e and Extended Fig. 10c). However,

550 individuals with variants impacting mRNA splicing in Groups 1 had significantly higher
551 standard adaptive behavior and socialization scores compared to Group 2 or 3
552 (Extended Fig. 10d, e). Interestingly, the NRXN1 gene that is part of group 2 has been
553 found to have alternative splicing in individuals with neuropsychiatric disorders⁸². This
554 suggests that splice variants may play a more prominent role in these groups with
555 respect to their effect on adaptive behavior and socialization scores. No significant
556 differences were seen between individuals with frame shift or stop gain variants in
557 genes from any group (Extended Fig. 10f, g), possibly due to the lower number of
558 individuals in the analyses, or an equally detrimental impact of these variants on all ASD
559 risk genes. The differences between Group 1 and Groups 2 or 3 suggest that PPI
560 networks can be used to cluster ASD-risk genes, and individuals with variants in those
561 genes. Group 1 genes were found to have the largest enrichment of ASD-risk genes
562 (Extended Fig. 10h), suggesting that the highly interconnected PPI networks and shared
563 pathways for this group of genes may be a core driver for the affected clinical
564 phenotypes (Extended Fig. 10h). The functional grouping of ASD-risk genes highlights
565 the potential of using PPI networks to correlate biological function with clinical
566 phenotype. This could lead to a better approach in subdividing individuals with ASD and
567 understanding the biological basis of these subgroups.

568 ***Discussion and Conclusion***

569 ASD is a heterogeneous group of neurodevelopmental disorders that are largely
570 caused by genetic variants in multiple risk genes²⁻⁵. A long-standing question in the field
571 is how different risk genes contribute to ASD, and whether there are convergent
572 signaling mechanisms that explain how a multitude of genes lead to a common, albeit
573 heterogeneous, developmental brain disorder. Specific disease cell types or signaling
574 pathways have been proposed as convergent mechanisms in ASD^{9,19,24-26}, but the bulk
575 of these data are based on RNA expression, which does not take into account signaling
576 at the protein level. To address this gap, we devised an *in vitro* neuron-specific
577 proteomic screen to identify individual and shared PPI networks between 41 ASD-risk
578 genes. Our screen identified links between risk genes and multiple convergent signaling
579 pathways. In addition, PPI network mapping could predict the functional impact of
580 disease-associated missense variants. Finally, PPI network mapping of ASD-risk genes
581 revealed an important relevance to human ASD pathology as the network enriched for
582 additional ASD risk genes and cell types implicated in ASD pathology. Cross-
583 referencing the PPI network with human clinical data revealed a biological link between
584 highly interacting ASD-risk genes and ASD diagnostic behavioral severity,
585 demonstrating the clinical relevance of the network.

586 While other approaches for identifying PPI networks exist, such as Y2H or affinity
587 purification coupled with mass spectrometry in cells lines, these methods can miss
588 weak and transient interactions and signaling networks specific to neurons^{31,32,83}. Our

589 use of BioID2 for the 41 ASD-risk genes revealed shared protein interactions which
590 include direct and indirect interactions between ASD-risk proteins in a neuronal cell
591 type, providing detailed insight into the relationship between the 41-risk proteins.
592 However, unlike these studies we used single canonical isoforms of each gene and
593 therefore some PPI networks may not encompass the full scope of possible interactions
594 in the neuron. Further, the mouse system possesses glial cells required for synaptic
595 maturation, and it is scalable; therefore, the system could be used to screen hundreds
596 of genes. Some caveats of BioID2 include possible biotinylation inefficiencies, protein
597 function impairments, and protein biotinylation selection biases, however, newer
598 proximity-labeling tools could be used to extend the identification of PPI networks^{84–87}.

599 Previous genetic screening platforms have identified shared pathways between
600 ASD-risk genes. CRISPR/Cas9 knockout screens have identified cell types and
601 processes associated with groups of ASD-risk genes^{20–22}. Since these knockout
602 screens disrupted genes early in development, this may skew results towards
603 neurogenesis deficits. Our BioID2 screen complement CRISPR/Cas9 approaches,
604 given that they can be used to study earlier or later time points, and can be used to
605 study disease-relevant variants. BioID2 can also help to understand the function or role
606 of poorly characterized ASD risk genes using our PPI network pipeline and statistical
607 cut-offs, where most previous studies rely on known compartment localization. Future
608 studies could also be used to study changes in disease-relevant PPI networks in
609 genetic mouse models or patient-derived iPSC neurons and organoids. Since changes
610 in protein interaction complexes or synaptic networks in multiple ASD mouse models
611 have been observed^{32,88}, this suggests that core ASD networks can reveal risk gene
612 clusters or identify hub genes.

613 One of the main findings from our study is the identification of multiple
614 convergent and shared pathways between 41 ASD-risk genes that are non-nuclear,
615 which fall into categories pertaining to synaptic transmission, TCA cycle and
616 mitochondrial activity, Wnt signaling, potassium channel activity, MAPK signaling, and
617 other specific signaling pathways. Synaptic transmission and function is widely known in
618 ASD pathophysiology, and Wnt and MAPK signaling have also been disrupted in ASD
619 patient cell lines⁸⁹. We focused on validating the TCA cycle and mitochondrial activity
620 pathways because its dysfunction is indirectly associated with neurodevelopmental
621 disorders⁹⁰ and our screen identified many uncharacterized ASD-risk genes associated
622 with this pathway (Fig. 3a). Clinical studies have found mitochondrial and metabolic
623 dysfunction or changes in metabolites in primary lymphocytes or brain tissue in
624 individuals with ASD^{55,56,91–96}, but whether this is direct or indirect is not known. A
625 mouse model expressing an mtDNA variant was shown to display autism associated
626 behavioral deficits⁹⁷, but the variant is weakly associated with ASD. Some ASD
627 associated syndromic disorders, co-morbid disorders and genetic ASD models have

628 shown deficits in mitochondrial and metabolic processes, however the specific proteins
629 involved were unknown^{52,53,105,54,98–104}. Our findings indicate that TCA cycle and
630 mitochondrial activity proteins are interacting with multiple ASD-risk genes, including
631 genes that were not previously connected to metabolic processes. While, two ASD-risk
632 genes (RHEB and BCKDK) have been previously implicated directly in metabolic
633 processes^{66,106}. This highlights that our screen can identify relevant protein interactions
634 and may even suggest a more direct connection between mitochondrial/metabolic
635 processes and some genetic models (CDKL5 and KCTD13)^{103,105}.

636 Our CRISPR/Cas9 KO studies revealed that multiple ASD-risk genes are
637 important for proper cellular respiration. Interestingly, these genes were all found to
638 interact with citrate synthase (Fig. 3a), suggesting that upstream or downstream
639 regulation may occur between ASD risk genes and TCA cycle function. Deficits in the
640 TCA cycle can cause overreliance on glutaminolysis to produce energy and cause a
641 decrease in synaptic vesicle glutamate levels^{107–109}. This shift may help explain the
642 deficits in synaptic transmission in neurons with disruption of synaptic ASD-risk genes,
643 such as *Syngap1* and *Taok2*. The shared PPI network provides an important link
644 between metabolic processes and ASD pathology. These data underscore the value of
645 using PPI networks to map ASD-risk gene connectivity, and to pinpoint which risk genes
646 are involved in convergent mitochondrial/metabolic dysregulation in ASD.

647 ASD-associated *de novo* missense mutations are enriched in hub genes of
648 known protein interaction networks^{30,110}. However, few studies have used proximity-
649 labeling to study the impact of disease-relevant mutations on the PPI network of genes
650 associated with neurodevelopmental or neurological disorders^{111–113}. Our BioID2 screen
651 provides functional evidence of the impact ASD-associated *de novo* missense variants
652 have on the PPI network of three ASD-risk genes, as examples. Time- and resource-
653 intensive studies have also investigated multiple variants in single genes in various
654 animal models^{114,115}. Additional bioinformatic approaches have been used to determine
655 the pathogenicity of rare missense variants; however, the impact on biological pathways
656 remains to be determined^{116,117}. Using neuron-specific PPI networks allows the use of a
657 relevant cell type, while being able to scale up the screen to test multiple single-gene
658 variants in a nonbiased manner and reduced period of time. This approach could have
659 potential applications for variants of unknown significance by providing important
660 information on the severity of a given genetic variant.

661 The enrichment of an additional 112 ASD risk genes in the shared ASD-risk gene
662 PPI network map and the enrichment of the network in ASD-associated cell types
663 further emphasizes the interconnectedness of ASD risk proteins. Mid-fetal deep cortical
664 projection neurons and superficial cortical glutamatergic neurons are enriched for ASD-
665 risk genes and are associated with autism pathology^{17,18}. The ASD-shared PPI network
666 was highly enriched for genes expressed in excitatory and inhibitory neurons, and for

667 DEGs in individuals with ASD specific to Layers 2/3 excitatory neurons and VIP
668 interneurons. The high connectivity and enrichment of ASD-risk genes within the
669 network reflect its relevance to shared pathways associated with ASD pathology. Future
670 studies will need to distinguish which ASD PPI networks are specific to each cell type,
671 or possible subpopulations, to understand the subtle network changes that impact
672 disease mechanisms.

673 Of great interest was the ability to group the 41 ASD-risk genes based on their
674 PPI network, and the correlation of these groups to clinical scores in adaptive behavior
675 and socialization. Although we focused specifically on missense/LoF variants, we found
676 that the type of variant in each group of genes had large effects on the average score of
677 the individuals within the group. To work through the complexity, it may be important to
678 combine our analysis with other methods of categorizing mutations (e.g. gnomAD pLI,
679 Polyphen-2) as higher or lower impact^{118,119}, which would reduce the number of people
680 shared between groups. Based on our findings, we highlight the ability to group ASD-
681 risk genes based on their PPIs and correlate the groups to differences in clinical scores
682 related to ASD.

683 In conclusion, our neuron-specific 41 ASD-risk gene PPI network map
684 demonstrates that protein signaling networks are relevant to ASD disease pathology,
685 and are missing from transcriptome-based approaches. Our approach is scalable and to
686 our knowledge, represents one of the largest protein network mapping studies for ASD
687 risk genes. This resource containing the individual PPI networks of 41 ASD-risk genes
688 will be valuable for future in-depth study of the genes, and has the potential to grow
689 larger with PPI networks of additional risk genes. Furthermore, the comparison of PPI
690 networks to large-scale human clinical and genetic datasets demonstrates a step
691 towards grouping ASD individuals and risk genes based on biological evidence.
692 Ultimately, the hope is that this approach may translate into a better understanding of
693 wide-ranging ASD clinical phenotypes and the development of targeted therapies.

694

695

696

697

698

699

700 **Material and Methods**

701

702 **Antibodies**

703 The following antibodies were used for immunostaining and immunoblotting
704 experiments: rabbit anti-FLAG (IB 1:2,000, MilliporeSigma, F7425), mouse anti-FLAG
705 (IF 1:1,000, IB: 1:2000, MilliporeSigma, F3165), rabbit anti-turboGFP (IF 1:1,000, IB
706 1:1,000, Fisher, PA5-22688), chicken anti-MAP2 (IF 1:1,000, Cedarlane, CLN182),
707 rabbit anti- β -actin (IB 1:1,000, Cell Signaling, 8457S), mouse anti- β -actin (IB 1:5,000,
708 MilliporeSigma, A5316), goat anti-TAOK2 α/β (IB 1:1,000, Santa Cruz Biotechnology, sc-
709 47447), rabbit anti-TAOK2 β (IB 1:1,000, Synaptic Signaling, 395 003), mouse anti-
710 Synapsin1 (IF: 1:1000, Synaptic Systems, 106 001), mouse anti-TOMM20 (IF 1:100,
711 US Biological, 134604), DAPI (IF 300mM, ThermoFisher, D21490), Hoechst (IF
712 1:10,000, Invitrogen, 1050083), Phalloidin-488 (IF 1:120, Cytoskeleton Inc., PHDG1),
713 Anti-mouse-Cy3 (IF 1:500, Jackson Immunoresearch, 715-165-151), Cy3 anti-mouse
714 (IF 1:500, Jackson Immunoresearch, 715-165-151), Alexa 488 anti-rabbit (IF 1:500,
715 Jackson Immunoresearch, 711-545-152), Alexa 488 anti-chicken (IF 1:500, Jackson
716 Immunoresearch, 703-545-155), 405 conjugated-streptavidin (IF 1:500, Jackson
717 Immunoresearch, 016-470-084), 405 anti-chicken (IF 1:500, Jackson Immunoresearch,
718 703-475-155), Alexa 647 anti-mouse (IF 1:500, Jackson Immunoresearch, 715-605-
719 150).

720

721 **Generation of constructs**

722 All cloning was accomplished using the In-Fusion HD cloning kit (Takara). To
723 create the BioID2 fusion constructs, we obtained an expression construct containing a
724 198bp (13x "GGGS" repeat) linker sequence upstream of a C-terminal 3xFLAG-
725 tagged BioID2 sequence with BioID2 (Genscript). For lentiviral expression, 13xlinker-
726 BioID2-3xFLAG was amplified and cloned into the lentiviral backbone pLV-hSYN-RFP
727 (Addgene #22909)¹²⁰. For ease of visualization and to create a bicistronic construct, the
728 RFP in the pLV-hSYN-RFP backbone was replaced with the TurboGFP(tGFP)-P2A
729 from pCW57-GFP-2A-MCS (Addgene #71783)¹²¹. NheI digest sites were added after
730 the P2A sequence and before the 13xLinker to allow easy insertion of ASD-risk bait
731 genes. The final construct being pLV-hSyn-tGFP-P2A-Bait-13xLinker-BioID2-3xFLAG
732 (referred to as the BioID2 fusion construct). For the control luciferase construct a
733 second P2A was cloned in between the luciferase ORF and the 13xLinker, creating the
734 pLV-hSyn-tGFP-P2A-Luciferase-P2A-13xLinker-BioID2-3xFLAG construct (referred to
735 as the Luciferase control construct). ASD-risk genes open reading frames (ORFs) were
736 purchased from Addgene and Genscript or amplified from human adult and fetal brain
737 RNA (Takara) (see Supplementary Table 10)^{122,123,132-139,124-131}. For mouse
738 electrophysiology experiments, the GRIA1, GRIA1 R208H and GRIA1 A636T ORFs
739 were inserted between the GFP-P2A and 3xFLAG. The pLV-CMV-Cas9-T2A-EGFP
740 plasmid was made by replacing the UBC promoter-rTetR in the FUW-M2rtTA plasmid
741 (Addgene #20342)¹⁴⁰ with CMV-Cas9-T2A-EGFP from PX458 (Addgene #48138)¹⁴¹. All
742 generated constructs are available upon request.

743

744

745

746 **Animal housing**

747 Taok2 Het (*Taok2 +/-*) and KO (*Taok2 -/-*) mice were created by Kapfhamer *et*
748 *al.*¹⁴². The E15-16 or E18 mouse embryo brains were used for cortical neuronal
749 cultures. P21-P23 mice were used for mass spectrometry or RNA sequencing
750 experiments. Animals housed at the Central Animal Facilities at McMaster University
751 were approved for experiments and procedures by the Animal Research Ethics Board
752 (AREB) at McMaster University. Animals housed at the University Medical Center
753 Hamburg-Eppendorf, Hamburg were approved for experiments and procedures by local
754 authorities of the city-state Hamburg (Behörde für Gesundheit und Verbraucherschutz,
755 Fachbereich Veterinärwesen) and the animal care committee of the University Medical
756 Center Hamburg-Eppendorf. All procedures were performed according to the German
757 and European Animal Welfare Act. Animals housed at the Animal Resource Center at
758 University Health Network were approved for experiments and procedures by the
759 University Health Network animal care committees.

760

761 **Mouse Cortical Neuron Cultures**

762 E15-E16 CD1 mice embryo cortices were harvested using a dissecting
763 microscope and kept in HBSS. Cortices were then digested in 300 µg/ml of papain
764 (Worthington) and 2 U/ml of DNase (Thermo) for 20 minutes at 37 °C. Cortices were
765 then washed three times with mouse plating media (Neurobasal media supplemented
766 with 2 mM GlutaMAX (Thermo), Pen-Strep (Thermo), and 10% FBS(Gibco)). Digested
767 cortices were triturated and put through 40 µm strainer. Cells were counted, suspended
768 in plating media, and plated at 600,000 cells per well of a 12-well plate. Plates were
769 coated with 100 µg/ml poly-D-lysine (mol wt > 300,000, Sigma) and 3 µg/ml Laminin
770 (Sigma). For immunostaining, 12 mm coverslips (Fisher) were placed in the well prior to
771 coating. The cells were incubated at 37 °C (with 5 % CO₂) for one hour, after which
772 plating media was removed and replaced with mouse culturing media (Neurobasal
773 media supplemented with 2 mM GlutaMAX, Pen-Strep, and B27). Cells were grown at
774 37 °C (with 5 % CO₂) and half media changes were done on day 7 and every 3-4 days
775 onwards.

776

777 **CRISPR/Cas9 editing of human induced pluripotent stem cells (iPSCs)**

778 All work with the human iPSCs was performed with the approval of the Hamilton
779 Integrated Research Ethics Board. Human iPSCs were maintained on Matrigel
780 (Corning) coated plates using mTeSR1 media (Stem Cell Technologies) and passaged
781 every 3-4 days using ReLeSR (Stem Cell Technologies). Human iPSCs were edited for
782 homozygous knockout of *TAOK2* or heterozygous knock-in of the A135P mutation as
783 described in Deneault *et al.*⁷⁰. MGB probes were ordered from ThermoFisher scientific
784 and ssODN were designed on Benchling.com (Biology Software) and ordered from
785 Integrated DNA Technologies. For the A135P mutation a mutant and wildtype ssODN
786 containing the A135P (G to C) mutation and a PAM site mutation or just the PAM site
787 mutation, respectively, were used to create a heterozygous knock-in.

788

789 **Human iPSC to neuron differentiation via NGN2 induction**

790 Human iPSCs were cultured on Matrigel (Corning) coated plates using mTeSR1
791 media (Stem Cell Technologies) and passaged every 3-4 days using ReLeSR (Stem

792 Cell Technologies) until neural induction. A modified NGN2 induction protocol (Zhang *et*
793 *al.* 2013) was used to differentiate human iPSCs into excitatory NGN2 neurons⁷².
794 Human iPSCs were dual infected with pTet-O-NGN2-P2A-EGFP and FUW-M2rtTA
795 lentiviruses for dox-inducible expression and were titered for > 90% infection efficiency.
796 On Day -1 iPSCs were singularized using Accutase (Stem Cell Technologies) and
797 plated with mTeSR1 media (supplemented with 10 μ M Y-27632) on Matrigel at 400,000
798 cells per well in a 6-well plate. On Day 0, media exchanged and supplemented with
799 Doxycycline (1 μ g/ml). On Day 1 and 2, media was replaced with iNPC media
800 (DMEM/F12 media (Gibco) supplemented with N2 (Gibco), MEM NEAA (Thermo), 2mM
801 GlutaMAX, and Pen-Strep) with Doxycycline and Puromycin (2 μ g/ml). On Day 3, media
802 was then replaced with iNi media (Neurobasal media with SM1 (Stem Cell
803 Technologies), 2mM GlutaMAX, Pen-Strep, 20 ng/ml BDNF, 20 ng/ml GDNF, and 1
804 μ g/ml Laminin) with Doxycycline. On day 4, differentiated neurons were singularized
805 using Accutase and re-plated at 100,000 cells per well in a 24-well plate in only iNi
806 media. Plates were pre-coated with 20 μ g/ml Laminin and 67 μ g/ml Poly-ornithine
807 (Sigma). Mouse glial cells were plated on top of the differentiated neurons after 24
808 hours at a density of 50,000 cells per well. Half-media changes were carried out every
809 other day, and iNi media was supplemented with 2.5 % FBS on Day 9 and onwards.
810 Neurons were grown until day 28 post NGN2-induction.

811

812 **Generation of high-titer lentivirus**

813 All viruses were made using the 2nd generation lentiviral packaging systems in
814 Lenti-X HEK293 FTT cells (Takara). Lenti-X cells were passaged maximum 3 times
815 before being used for virus production in HEK media (High glucose DMEM with 4 mM
816 GlutaMAX, 1 mM Sodium Pyruvate, and 10 % FBS). Lenti-X cells were passaged once
817 with 500 μ g/ml Gentamycin (Thermo) to increase T antigen expressing cells. Cells were
818 plated into T150 flasks and each flask was transfected with the BioID2 lentiviral plasmid
819 and the packaging plasmids, pMD2.G and pPAX2 (Addgene #12259 and #12260),
820 using Lipofectamine 2000 in a 3:5 Opti-MEM: HEK media mix. Media was exchanged
821 for fresh media after 5.5-6 hours. Media was harvested twice, first at 48 hours and then
822 at 72 hours post-transfection and spun at 100,000xG for 2 hours (maximum acceleration
823 and deceleration). The virus was resuspended in PBS and kept at -80°C until they were
824 used. Larger and unstable viruses were spun at 20,000xG for 4 hours in a table top
825 centrifuge using a 20 % sucrose cushion¹⁴³. See nature exchange protocol for detailed
826 procedure.

827

828 **Infection of mouse cortical neurons for BioID2 screen**

829 One plate of 7.2 million mouse cortical neurons was considered as one biological
830 replicate. Each cortical neuron culture produced at least 5 plates for four separate
831 BioID2 bait gene samples and one luciferase control sample. Three separate cultures
832 were done in a 3 days span in one week to get 3 biological replicates per protein-of-
833 interest (POI). On days *in vitro* (DIV) 14, the conditioned media from the mouse neuron
834 cultures were removed, leaving only 0.5 ml of media per well. Extra wells with and
835 without coverslips were infected at the same MOI for flow cytometry measurements of
836 GFP positive neurons and immunostaining, respectively. On DIV14, lentivirus with
837 BioID2 fusion constructs were added to each well at an MOI of 0.7 and on DIV17 each

838 well was supplemented with 50 μ M of Biotin. After 18-20 hours, cells for mass
839 spectrometry were lysed with RIPA buffer (1 % NP40, 50 mM Tris-HCl, 150 mM NaCl,
840 0.1 % SDS, 0.5 % deoxycholic acid, and protease inhibitor cocktail (PIC)) and flash
841 frozen in liquid nitrogen. Cells for flow cytometry were dissociated with 0.25 % Trypsin-
842 EDTA (Fisher) and resuspended in PEF media (PBS with 2 mM EDTA and 5 % FBS)
843 (See flow cytometry section). Cells for immunostaining were fixed with 4 % PFA for 20
844 minutes, washed with PBS, and kept at 4 °C for staining.

845

846 **Transfection of HEK293 FT cells for BioID2 screen**

847 10 million HEK293 FT cells were plated in a 10 cm culture dish and transfected
848 24 hours later with the BioID2 fusion construct plasmids using Lipofectamine 2000.
849 Media was changed 6 hours after transfection and 50 μ M biotin was added 48 hours
850 post-transfection. Cells were lysed 72 hours post-transfection in RIPA buffer and flash
851 frozen in liquid nitrogen. Each individual plate was considered as biological replicate
852 and three plates were used for each gene and the luciferase control. An extra plate was
853 used for flow cytometry measurements of GFP positive cells.

854

855 **Processing of mouse cortical neuron and HEK293 FT cell BioID2 samples**

856 Lysed cells were thawed and DNA was digested using benzonase (Sigma).
857 Lysates were then sonicated at high speed for 5 seconds and centrifuged at 20,000xG
858 for 30 minutes. The lysate supernatants were incubated with streptavidin Sepharose
859 beads (GE Healthcare) at 4 °C for 3 hours. Following the incubation, the supernatant
860 was spun down at 100xG for 2 minutes and the supernatant was removed. The beads
861 were then washed once with RIPA buffer, and then six times with 100 mM
862 triethylammonium bicarbonate (TEAB) with centrifugation between each wash. After the
863 final wash, the beads are then resuspended in 100 mM TEAB and sequencing-grade
864 trypsin (Promega) was added to digest the biotinylated proteins on the beads into
865 peptides. The beads were incubated at 37 °C for 16 hours while rotating, and additional
866 trypsin was added and incubated for a further 2 hours. The beads were then pelleted
867 and the supernatant was transferred to a new tube. The beads were washed twice with
868 100 mM TEAB and each wash was added to the supernatant. The supernatant was
869 then transferred to a 1.5 mL screw cap tub and speed vacuum dried. The dried peptides
870 were stored at 4 °C for TMT-labeling.

871

872 **Multiplex TMT-labeling of BioID2 samples**

873 Dried peptides were resuspended in 100 mM TEAB. Each sample was TMT-
874 labeled using the TMT 10plex Isobaric Mass Tagging Kit (Thermo). The four genes
875 (proteins-of-interest, POI) were divided into two separate batches and the luciferase
876 control samples were divided between the batches. Each batch had three biological
877 replicates of the two genes and the luciferase control. One luciferase sample chosen at
878 random was divided and labeled with two different labels to determine variance due to
879 labeling efficiencies. In brief, TMT-label resuspended in acetonitrile was added to each
880 sample and incubated at room temperature for one hour. To stop the reaction, 5 %
881 hydroxylamine was then added to the samples and incubated for 15 minutes at room
882 temperature. All ten samples were combined into one tube and divided into two

883 samples. Both samples were then speed vacuum dried. One sample was kept at -80 °C
884 for storage and the second sample was kept at 4 °C to be run in the mass spectrometer.

885 886 **Identification of biotinylated proteins from BioID2 screen samples using LC-** 887 **MS/MS**

888 Peptide samples were resuspended in 0.1% Trifluoroacetic acid (TFA) and
889 loaded for liquid chromatography, which was conducted using a home-made trap-
890 column (5 cm x 200 µm inner diameter; POROS 10 µm 10R2 C18 resin) and a home-
891 made analytical column (50 cm x 50 µm inner diameter; Monitor 5 µm 100A C18
892 resin), running a 120min (label free) or 180min (TMT) reversed-phase gradient at
893 70nl/min on a Thermo Fisher Ultimate 3000 RSLCNano UPLC system coupled to a
894 Thermo QExactive HF quadrupole-Orbitrap mass spectrometer. A parent ion scan was
895 performed using a resolving power of 120,000 and then up to the 20 most intense peaks
896 were selected for MS/MS (minimum ion count of 1000 for activation), using higher
897 energy collision induced dissociation (HCD) fragmentation. Dynamic exclusion was
898 activated such that MS/MS of the same m/z (within a range of 10 ppm; exclusion list
899 size = 500) detected twice within 5 seconds were excluded from analysis for 30
900 seconds. Data were analyzed using Proteome Discoverer 2.2 (Thermo). For protein
901 identification, search was against the Swiss-Prot mouse proteome database (55,366
902 protein isoform entries)¹⁴⁴, while the search parameters specified a parent ion mass
903 tolerance of 10 ppm, and an MS/MS fragment ion tolerance of 0.02 Da, with up to two
904 missed cleavages allowed for trypsin. Dynamic modification of +16@M was allowed.

905 906 **Analysis for the identification of ASD-risk and cellular compartment protein PPI** 907 **networks**

908 Only proteins identified with two unique peptides were used for analysis. Flow
909 cytometry was used to calculate the total GFP in infected neuron samples. If the POI
910 sample had less GFP than the luciferase control sample, the factor needed to equalize
911 the amount of GFP was applied to the protein abundances of the POI samples. Protein
912 abundances were also normalized to the highest total protein count sample for each set
913 of biological replicates. Unpaired one-tailed student's test was used to determine
914 significantly enriched biotinylated proteins in the POI sample using the Log2
915 abundances of the three biological replicates of the POI samples compared to the
916 luciferase control samples ($p < 0.05$)³⁶. Significance B outlier test was used to identify
917 significantly biotinylated proteins in the POI sample compared to the luciferase control
918 sample using the average abundance and protein abundance ratio between POI and
919 luciferase samples (SigB $p < 0.05$). Only proteins that were found to be significant from
920 both analyses were included in the PPI network. The protein abundance ratio between
921 the luciferase control replicate samples, which were labeled with different TMT labels,
922 was considered to be the minimal ratio required for significance. Any protein that did not
923 surpass this ratio was considered to be a false positive, even if statistically significant,
924 and not included in the PPI network.

925 926 **Pathway enrichment analyses**

927 All pathway enrichment analysis was done using the g:Profiler GOst functional
928 profiling tool (<https://biit.cs.ut.ee/gprofiler/gost>)¹⁴⁵. We used internal sources without

929 electronic GO annotations for GO biological processes and GO cellular component
930 (compartment), and curated Reactome pathway gene sets from the Bader lab
931 (http://download.baderlab.org/EM_Genesets/)¹⁴⁶. All three sources were used for the
932 shared ASD-risk gene network proteins. Only GO cellular component enrichment was
933 used for the HEK293 FT cell BioID2 PPI networks, neuron cellular compartment BioID2
934 PPI networks, and *de novo* missense mutation network BioID2 PPI network
935 comparisons. We compared the protein lists against a custom statistical domain of
936 proteins identified through fractionated mass spectrometry of the mouse brain¹⁴⁷ and
937 combined with any additional proteins identified in the BioID2 screen. The final mouse
938 brain proteome background had a total of 11992 proteins after removing multiple
939 isoforms of the same protein. HEK293 BioID2 PPI networks were compared to all
940 annotated gene lists. The g:Profiler Benjamini-Hochberg FDR multiple correction was
941 used and only pathways with an adj. p-value < 0.05 were considered significantly
942 enriched. For cellular component enrichment for *de novo* missense variant BioID2 PPI
943 networks, the ggplot package in R was used to create the dot plots. For *de novo*
944 missense variant BioID2 bait genes, all proteins identified in the wildtype samples were
945 used for analysis, while for the shared PPI network map only proteins found in all
946 wildtype samples were used for pathway enrichment analysis.

947

948 **Virus titering and GFP normalization for BioID2 screen**

949 Mouse cortical neurons were cultured as described above and infected on DIV3
950 at three dilutions of virus (1:100, 1:333, 1:1000). On DIV 5, infected mouse cortical
951 neurons were singularized using 0.25 % Trypsin-EDTA (Fisher) and resuspended in
952 PEF media (PBS with 2 mM EDTA and 5 % FBS). For GFP normalization, DIV18
953 mouse neurons infected with the BioID2 lentiviruses were dissociated with Trypsin and
954 resuspended in PEF media. CytoFLEX-LX or CANTO II flow cytometers were used to
955 measure the percentage of GFP-positive cells with the 488 laser and 525/40 or 525/50
956 filters, respectively, using CytExpert software (Beckman Coulter). Functional titers were
957 calculated based on the linear relationship between virus amount and percent of GFP
958 positive cells. Mouse cortical neurons were infected at an MOI of 0.7, where 70 percent
959 of cells were expected to be infected with the BioID2 lentiviral constructs. For
960 normalization, the total GFP per 20,000 GFP-positive cells were quantified by taking the
961 area under the GFP intensity histogram. GFP percentage and total amount was
962 calculated using FlowJo software.

963

964 **Western blots**

965 HEK293 FT cells were transfected with the BioID2 constructs using
966 Lipofectamine 2000 (Invitrogen) in Opti-MEM: HEK media. Cells were harvested 48
967 hours post-transfection and lysed with RIPA buffer (with fresh PIC). Lysates were either
968 snap-frozen in liquid nitrogen or taken directly for western blot sample preparation.
969 Thawed or fresh lysates were sonicated at high frequency for 5 seconds and
970 centrifuged at 20,000xG for 5 minutes at 4 °C. Lysates were then quantified using the
971 Bio-Rad Bradford protein assay (Bio-Rad) by measuring absorbance with the
972 SPECTROstar Nano machine and MARS Data analysis software (BMG LABTECH) and
973 diluted to equal concentrations with RIPA buffer. 30-50 µg of protein were run on 8 % or
974 10 % SDS-PAGE Tris-Glycine gels (depending on the size of the proteins) at 100V for

975 initial stacking and then 140V for 1-1.25 hours in a Tris-Glycine running buffer. Proteins
976 were then transferred onto PVDF membrane using a Tris-Glycine buffered wet transfer
977 system for 2 hours at constant 200 mA. Blots were then blocked with 5% milk in TBS-T
978 (Tris buffered saline pH 7.4 with 0.1 % Tween). Blots were incubated with primary
979 antibodies overnight in 5 % milk/TBS-T. The next day, membranes were washed three
980 times with TBS-T for 5 minutes each and then incubated with secondary antibodies in 5
981 % milk/TBS-T for 1 hour. Blots were imaged by incubating them with the Amersham
982 ECL western blotting detection reagent (VWR) for 1 minute and then imaging every 10
983 seconds for 5 minutes on the ChemiDoc XRS+ machine (Bio-Rad). ImageLab (Bio-Rad)
984 was used for band intensity quantification.

985 986 ***In vitro* whole-cell patch clamp recordings of human iPSC-derived neurons and** 987 **mouse cortical neurons**

988 Human iPSC-derived neurons were used for electrophysiology experiments
989 between days 21-24 of the neural differentiation protocol. Whole-cell patch-clamp
990 recordings were performed at room temperature using Multiclamp 700B amplifier
991 (Molecular Devices) from borosilicate patch electrodes (P-97 puller and P-1000 puller;
992 Sutter Instruments) containing a potassium-based intracellular solution (123 mM K-
993 gluconate, 10 mM KCl, 10 mM HEPES; 1 mM EGTA, 1 mM MgCl₂, 0.1 mM CaCl₂, 1
994 mM Mg-ATP, and 0.2mM Na₄GTP, pH 7.2). 0.06% sulpharhodamine dye was added to
995 the intracellular solution to confirm the selection of multipolar neurons. The extracellular
996 solution consisted of 140 mM NaCl, 5 mM KCl, 1.25 mM NaH₂PO₄, 1 mM MgCl₂, 2 mM
997 CaCl₂, 10 mM glucose, and 10 mM HEPES (pH 7.4). Data was digitized at 10 – 20 kHz
998 and low-pass filtered at 1 - 2 kHz. Recordings were omitted if access resistance was
999 >30 MΩ. Whole-cell recordings were clamped at -70 mV and corrected for a calculated -
1000 10mV junction potential. Rheobase was determined by a step protocol with 5 pA
1001 increments, where the injected current had 25 ms duration. Action potential waveform
1002 parameters were all analyzed in reference to the threshold. Repetitive firing step
1003 protocols ranged from -20 pA to +50 pA with 5 pA increments. No more than two
1004 neurons per coverslip were used to reduce the variability. Data were analyzed using the
1005 Clampfit software (Molecular Devices), while phase-plane plots were generated in the
1006 OriginPro software (Origin Lab). For GRIA1 overexpression experiments, mouse
1007 neurons were infected with GRIA1, GRIA1 R208H, and GRIA1 A636T lentiviral
1008 constructs at DIV11 and recorded on DIV14-15. Mouse neurons for electrophysiology
1009 experiments were cultured in Neurobasal media (supplemented with an additional 0.3 %
1010 (w/v) glucose and 0.22 % (w/v) NaCl). The same intracellular solution was used as the
1011 human neuron recordings, with a mouse artificial cerebrospinal fluid extracellular
1012 solution (125 mM NaCl, 2.5 mM KCl, 2 mM CaCl₂, 1 mM MgCl₂, 5 mM HEPES, 33 mM
1013 Glucose, pH 7.2). Whole-cell recordings of mouse neurons were clamped at -80 mV
1014 and corrected for a calculated -10mV junction potential.

1015 1016 **Staining and imaging of mouse cortical neurons and human iPSC-derived** 1017 **neurons**

1018 Mouse cortical neurons and human iPSC-derived neurons on coverslips were
1019 fixed with 4% paraformaldehyde (PFA) for 10 minutes at room temperature, washed
1020 once with PBS, and stored in PBS at 4 °C protected from light. Fixed coverslips were

1021 then blocked and permeabilized in BP solution (PBS with 10% donkey serum and 0.3%
1022 Triton-X) for 45 minutes at room temperature. Coverslips were then incubated with
1023 primary antibodies at 4 °C overnight. The following day, coverslips were washed three
1024 times with PBS for eight minutes each. Coverslips were then incubated with secondary
1025 antibodies for one hour at room temperature, followed by three washes with PBS. For
1026 human iPSC-derived neuron Synapsin1 staining, coverslips were incubated with 300
1027 mM of DAPI for 15 minutes, before the third wash with PBS. Excess liquid was then
1028 removed from the coverslips and they were mounted onto VistaVision glass microscope
1029 slides (VWR) with 10 µL of Prolong Gold Anti-Fade mounting medium (Life
1030 Technologies). For TOMM20 staining, mouse neurons were fixed with 4% PFA at 37°C
1031 for 10 min and then permeabilized with 0.5 % Triton X-100 for 10 minutes. Non-specific
1032 binding was blocked by incubation with 5 % donkey serum in PBS for 50 minutes at
1033 room temperature, followed by primary antibody incubation. The secondary antibody
1034 was added for 50 minutes at room temperature. Primary and secondary antibodies were
1035 diluted in PBS with 0.5 % BSA, 2.5 % Donkey-serum, and 0.15 % Triton X-100. After
1036 primary and secondary antibody incubation, three washing steps with PBS were
1037 performed. Then, coverslips were incubated with Phalloidin-488, for F-actin labeling,
1038 and Hoechst dye for 45 minutes at room temperature followed by three PBS washes.
1039 Coverslips were mounted onto slides using Fluoromount-G® (Southern Biotech) and
1040 were stored protected from light. Synapsin1 and BiID2 stained images were taken on
1041 the Zeiss LSM 700 confocal microscope with 63x or 40x oil objective, respectively. Mito-
1042 dsRed images were taken on the Echo Revolve microscope with a 20x objective.

1043

1044 **Synapsin1 puncta analysis in human iPSC-derived neurons**

1045 Synapsin1 stained images were processed and analyzed with ImageJ software.
1046 The Synapsin1 antibody was co-immunostained with MAP2 to determine dendrites with
1047 presynaptic puncta. Five biological replicates, which represent five separate neural
1048 inductions, were used for synaptic analysis. 5-10 neurons per genotype per replicate
1049 were used. Imaging settings were kept the same between images and synapsin1
1050 images were analyzed at the same threshold. Dendrites were traced using ImageJ and
1051 the measure tool was used to quantify the number and size of the puncta within the
1052 traced region.

1053

1054 **Proteomic profiling of *Taok2* KO mice cortical post-synaptic density fraction 1055 through LC-MS/MS**

1056 The right cortical lobes of three P21-23 *Taok2* KO mice and five P21-23 wildtype
1057 littermates were harvested and differential centrifugation was used to obtain the crude
1058 post-synaptic density fraction¹⁴⁸. PSD fractionations were validated by western blot for
1059 PSD-95 and synaptophysin (data not shown). Final post-synaptic density pellets were
1060 resuspended using 8 M urea and 100 mM ammonium bicarbonate. Protein samples
1061 were then reduced with 10 mM Tris(2-carboxyethyl)phosphine for 45 min at 37 °C,
1062 alkylated with 20 mM iodoacetamide for 45 min at room temperature, and digested by
1063 trypsin (Promega) (1:50 enzyme-to-protein ratio) overnight at 37 °C. The peptides were
1064 desalted with the 10 mg SOLA C18 Plates (Thermo Scientific), dried, and labeled with
1065 Multiplex 10-plex TMT labels (Thermo) in 100 mM triethylammonium bicarbonate, and
1066 quenched with 5% hydroxylamine before combined. 40 µg of the pooled sample was

1067 separated into 60 fractions by high-pH reverse-phase liquid chromatography (RPLC)
1068 using a homemade C18 column (200 μm \times 30 cm bed volume, Waters BEH 130 5 μm
1069 resin) running a 70 min gradient from 11 to 32% acetonitrile– 20 mM ammonium
1070 formate (pH 10) at a flow rate of 5 $\mu\text{L}/\text{min}$. Each fraction was then loaded onto a
1071 homemade trap column (200 μm \times 5 cm bed volume) packed with POROS 10R2 10 μm
1072 resin (Applied Biosystems), followed by a homemade analytical column (50 μm \times 50 cm
1073 bed volume) packed with Reprosil-Pur 120 C18-AQ 5 μm particles (Dr. Maisch) with an
1074 integrated Picofrit nanospray emitter (New Objective). LC-MS experiments were
1075 performed on a Thermo Fisher Ultimate 3000 RSLCNano UPLC system that ran a 3 h
1076 gradient (11– 38% acetonitrile–0.1% formic acid) at 70 nL/min coupled to a Thermo
1077 QExactive HF quadrupole-Orbitrap mass spectrometer. A parent ion scan was
1078 performed using a resolving power of 120 000; then, up to 30 of the most intense peaks
1079 were selected for MS/MS (minimum ion counts of 1000 for activation) using higher
1080 energy collision-induced dissociation (HCD) fragmentation. Dynamic exclusion was
1081 activated such that MS/MS of the same m/z (within a range of 10 ppm; exclusion list
1082 size = 500) detected twice within 5 seconds was excluded from the analysis for 30
1083 seconds. Data were analyzed using Proteome Discoverer 2.2 (Thermo). For protein
1084 identification, search was against the SwissProt mouse proteome database (55,366
1085 protein isoform entries), while the search parameters specified a parent ion mass
1086 tolerance of 10ppm, and an MS/MS fragment ion tolerance of 0.02Da, with up to two
1087 missed cleavages allowed for trypsin. Dynamic modification of +16@M was allowed.
1088 Only proteins with two unique peptides were used for further analysis. Differentially
1089 expressed proteins (DEPs) were calculated through Significance B outlier test using the
1090 Perseus software¹⁴⁹, and only proteins that had adj. p-value < 0.05 were considered as
1091 DEPs.

1092 1093 **Transcriptome profiling of *Taok2* KO mice cortices through RNA sequencing**

1094 Cortices from *Taok2* KO and wildtype littermates were also harvested for RNA at
1095 post-natal day 21-23, with 3 males and 3 females from each genotype. The RNA was
1096 extracted using Trizol and was sent for total RNA sequencing at the Center for Applied
1097 Genomics (TCAG). mRNA was purified using poly(A) selection to avoid contamination
1098 of ribosomal RNAs and miRNAs. All samples were run on one lane resulting in ~31-34
1099 million of read pairs per sample. All analysis was carried out using the open-source
1100 platform Galaxy (usegalaxy.org)¹⁵⁰. RNA reads were checked for good quality using the
1101 FastQC tool. The trimmomatic tool was used to identify and trim off known adaptors and
1102 remove any bases that have a Phred score of less than 20. FastQC was used again to
1103 ensure that adaptor sequences were removed and that the quality of the reads was not
1104 affected. We next used the HISAT2 alignment program for alignment of the RNA
1105 sequences to the mouse genome GRCm38 (NCBI). On average 85% of reads from
1106 mouse samples were aligned once and 5% were aligned more than once to distinct
1107 genome locations. Moving on, the featureCounts tool was used to count the number of
1108 reads per gene using the same reference genome as the HISAT2 tool. The DESeq2
1109 tool was used to determine the significant differentially expressed genes (DEGs)
1110 between *Taok2* WT and KO mouse cortices. Genes were considered as DEGs if they
1111 had an adjusted p-value lower than 0.05.

1112

1113 **Gene set enrichment analysis (GSEA) of *Taok2* KO mouse proteome and**
1114 **transcriptome**

1115 DEGs and DEPs were ranked based on the equation $-\log_{10}(\text{adj. p-value}) * \text{Ln}(\text{fold}$
1116 $\text{change})$. GSEA 4.1.0 (Broad Institute)^{151,152} was used to run the GSEA preranked test.
1117 Tests were run with 1000 permutations, weighted enrichment statistics, and excluding
1118 gene sets smaller than 15 and larger than 500 genes. All other settings were kept as
1119 default. All mouse GO term gene sets without electronic GO annotations
1120 (http://download.baderlab.org/EM_Genesets/) were used for the analysis¹⁴⁶.
1121 Visualization of the enriched gene sets was done on Cytoscape 3.8.2 using the
1122 EnrichmentMap app and the AutoAnnotate app was used for clustering similar gene
1123 sets^{153–155}. All visualized gene sets had an FDR < 0.1.

1124

1125 **Seahorse assay of *in vitro* mouse and human iPSC-derived neurons**

1126 Mouse cortical neurons were cultured as described above at a density of 30,000
1127 cells/well in the Seahorse XF96 cell culture microplate. CRISPR/Cas9 KO mouse
1128 neurons were infected at DIV 7 and assayed at DIV 14. Human iPSC-derived NGN2
1129 neurons were plated on day 4 of dox induction at a density of 50,000 cells per well in
1130 the Seahorse XF96 cell culture microplates (Agilent), pre-coated with 20 $\mu\text{g/ml}$ Laminin
1131 and 67 $\mu\text{g/ml}$ Poly-ornithine (Sigma). Mouse glia was plated on top of the neurons at a
1132 density of 25,000 cells per well, 24 hours later. Cells were used for the Seahorse assay
1133 on day 7. The day prior to the seahorse assay the Seahorse XFe96 sensor cartridge
1134 was filled with Calibrant XF solution and incubated at 37 °C (without CO₂) overnight. On
1135 the day of the assay the Seahorse XF96 microplates were washed twice with 200 μl per
1136 well of pre-warmed MST media (Seahorse XF DMEM pH 7.4 media supplemented with
1137 1 mM sodium pyruvate, 2.5 mM GlutaMAX, and 17.5 mM Glucose). The plate was then
1138 filled with 180 μl per well MST media and incubated at 37 °C (without CO₂) for 1 hour.
1139 During the incubation, the mitochondrial stress test drugs were added to the XFe96
1140 sensor cartridge (1 μM Oligomycin for mouse neurons and 3 μM Oligomycin for human
1141 neurons, 1 μM FCCP, and 1 μM Rotenone/Antimycin A resuspended in MST media).
1142 The cartridge plate with the drug compounds were then put in the Seahorse XFe96
1143 analyzer for calibration. After calibration, the microplate was placed into the Seahorse
1144 XFe96 analyzer for the pre-set mitochondrial stress test protocol. Oxygen consumption
1145 rates (OCR) were recorded every seven minutes and the drug compounds were added
1146 in 21-minute intervals. Oligomycin was used to inhibit ATP-synthase to measure ATP-
1147 synthase dependant respiration, FCCP was added to decouple the inner membrane to
1148 measure maximal respiration, and Rotenone and Antimycin A were added together to
1149 measure non-mitochondrial respiration. After the assay, microplates were frozen at -
1150 80°C overnight and cell content was measured using the Cyquant cell proliferation
1151 assay (Thermo) by measuring fluorescence with the CLARIOStar machine and MARS
1152 data analysis software (BMG LABTECH). Cellular respiration analysis was performed
1153 using the Wave software (Agilent) and OCR values were normalized to the number of
1154 cells per well.

1155

1156 **CRISPR/Cas9 knockout in mouse cortical neurons**

1157 Mouse cortical neurons were infected at DIV7 with the pLV CMV-Cas9-T2A-
1158 EGFP (MOI 1) and pLV U6-sgRNA/EF1a-mCherry (MOI 3) lentiviruses. Cultures were

1159 allowed to recover until DIV14 and were then taken for the seahorse assay. The
1160 GeneArt genomic cleavage detection kit (Thermo) was used to detect insertions or
1161 deletions in the targeted sites.

1162

1163 **Measuring mitochondrial activity in shRNA knockdown mouse neurons**

1164 Embryonic age E15 C57BL6/J mouse pups were *in utero* electroporated with
1165 Taok2 shRNA and control shRNA. Electroporated mouse embryo cortices were then
1166 harvested and cultured at E18. Mouse neuron cultures were imaged at DIV5 after
1167 incubation with 2nM TMRM (Thermo). Images were analyzed on ImageJ. Soma regions
1168 were delineated and integrated density in the soma (soma area x mean intensity) was
1169 measured. For background correction, mean background intensity was obtained from
1170 the neighbouring region.

1171

1172 **Measuring mitochondrial activity and content in mouse cortical neurons**

1173 DIV 6 mouse cortical neurons cultured from *Taok2* WT, Het, and KO mouse
1174 embryos were incubated with 2 nM TMRM (Invitrogen, #T668) and/or 100 nM
1175 MitoTracker Green (Cell Signaling Technology, #9074P) were directly added to the
1176 conditioned medium, and incubated for 15 minutes. Cells were then imaged within 30
1177 minutes after the incubation time. Images were loaded onto ImageJ, background mean
1178 intensity was measured from the region without TMRM and MitoTracker signals inside
1179 the cell, then the cell was delineated and the background was removed. After
1180 background correction, using the JACoP plugin the TMRM-MitoTracker signal
1181 colocalization was analyzed using Manders' correlation coefficients. For Manders'
1182 correlation coefficients, threshold values for TMRM (red channel) and MitoTracker
1183 (green channel) were set to 335 ± 55 and 640 ± 50 respectively. 16-bit wide field images
1184 were taken on a Nikon EclipseTi2 inverted spinning disk microscope equipped with 60X
1185 oil (NA 1.4) objective, an LED light source (Lumencor® from AHF analysentechnik AG,
1186 Germany), and a digital CMOS camera (ORCA-Flash4.0 V3 C13440-20CU from
1187 Hamamatsu) controlled with NIS-Elements software. The microscope imaging chamber
1188 is equipped to maintain 37 °C temperature and 5 % CO₂. Illumination, exposure and
1189 gain settings were kept the same across different conditions for imaging TMRM and
1190 MitoTracker signals.

1191

1192 **TOMM20 staining analysis for mitochondria content in mouse cortical neurons**

1193 DIV 7-8 mouse cortical neurons cultured from *Taok2* WT, Het, and KO mouse
1194 embryos were fixed and stained for TOMM20. 16-bit Z-series images with a step size of
1195 300 nm Images were acquired on confocal spinning disk microscope using a 60X oil
1196 (NA 1.4) objectives. Illumination, exposure and gain settings were kept the same across
1197 the conditions. The images were loaded onto ImageJ and z-projection (sum slices) for
1198 the entire cell in z-axis was performed on the confocal images. Using ImageJ, soma
1199 region was carefully delineated and total intensity, also known as integrated density, in
1200 the soma (soma area * mean intensity) was measured. For background correction,
1201 mean intensity (background mean intensity) was obtained from the neighbouring region
1202 (out of the cell). Using the following equation, we obtained the corrected values.
1203 Corrected value = total intensity in the soma – (background mean intensity * soma
1204 area).

1205 **Electron microscopy of synaptic mitochondria from mouse brain cortices**

1206 Coronal vibratome sections of the cingulate cortex (cg1 and cg2) and the
1207 prelimbic cortex (PL) of the PFC, the primary somatosensory regions S1HL, S1FI,
1208 S1BF, and the intermediate HC were collected and prepared for electron microscopy as
1209 described in Richter *et al.*⁵⁹. Semithin sections (0.5 µm) were prepared for light
1210 microscopy mounted on glass slides and stained for 1 min with 1% Toluidine blue.
1211 Ultrathin sections (60 nm) were examined in an EM902 (Zeiss, Munich, Germany).
1212 Pictures were taken with a MegaViewIII digital camera (A. Tröndle, Moorenweis,
1213 Germany). EM images that were collected and analyzed for synapse formation on the
1214 dendritic spines or shafts from Richter *et al.* were reanalyzed for mitochondrial
1215 morphology. Mitochondria morphology from the EM images obtained from Taok2 Wt
1216 and Taok2 KO genotypes were analyzed manually using ImageJ. based on their
1217 morphology the mitochondria are and categorized to Category 1 - Normal mitochondria
1218 with well stacked Cristae, Category 2 - mitochondria with enlarged Cristae, Category 3 -
1219 mitochondria with condensed Cristae.

1220

1221 **Mito7-dsRed puncta analysis in human iPSC-derived neurons**

1222 TAOK2 KO, A135P and wildtype human iPSC-derived NGN2 neurons were
1223 transfected with 0.8 µg of Mito7-dsRed (Addgene #55838) and 0.2 µg of pCAG-Venus
1224 at day 5, with 2 µl of Lipofectamine 2000 (Thermo). Venus was used to trace neuron
1225 projections. 10 neurons per genotype from two separate neural inductions were used for
1226 analysis. Imaging settings were kept the same between images and Mito7-dsRed
1227 images were analyzed at the same threshold. Dendrites were traced using ImageJ and
1228 the measure tool was used to quantify the size of the puncta within the traced region
1229

1229

1230 **Correlation of 41 ASD-risk gene PPI networks**

1231 Corrplot (R package) was used to create the correlation plot. The normalized
1232 biotinylation score to the bait protein was used to calculate the correlation between
1233 ASD-risk gene PPI networks. The Silhouette and Within cluster sum of squares
1234 methods were used to calculate the optimal kmeans number for clustering. Genes were
1235 ordered by hierarchal clustering.

1236

1237 **Cell type/DEG/ASD gene list enrichment analysis**

1238 Human cell type gene expression and ASD DEGs and ASD gene lists were
1239 obtained from their respective publications^{11–16,25,43}. For the enrichment analysis we
1240 used the Fisher exact test comparing each gene list with the shared ASD-risk gene PPI
1241 network in the mouse brain background protein list, which was used for pathway
1242 enrichment analysis. P-values and ODDs ratios were calculated for each comparison.
1243 To account for multiple comparisons, Bonferroni correction thresholds were calculated
1244 as $p = 0.05$ divided by the number of comparisons.

1245

1246 **Clinical score analysis**

1247 Rare variants of individuals diagnosed with ASD were extracted from the
1248 MSSNG database (research.mss.ng)¹², which has whole genome sequences of 4,258
1249 families and 5,102 ASD-affected individuals. Only variants with estimated high or
1250 medium impact strengths were used for analysis, and variants were categorized into

1251 three groups (missense variants, splicing variants, and frame shift/premature stop
1252 codon variants). Adaptive behavior and socialization standard scores of affected
1253 individuals was extracted from the MSSNG associated Metabase (data-
1254 explorer.mss.ng). Individuals were grouped based on the presence of mutations in the
1255 41 ASD-risk genes that were clustered into three groups. Individuals that had variants in
1256 genes between multiple groups were not included in the analysis. Separate analyses
1257 were carried out between individuals grouped by missense, splicing or frame
1258 shift/premature stop codon variants. Clinical data was considered as non-parametric
1259 and the Kruskal-Wallis ranked test with post hoc Dunn's test was used for comparison
1260 between the adaptive behavior and socialization standard scores of each group.

1261

1262 **Data representation and figure generation**

1263 Networks and gene set enrichment maps were created on Cytoscape v3.8.2. Graphs
1264 were created on GraphPad Prism 7. Representative electrophysiology traces were
1265 extracted onto CoreIDRAW. Microscopy images were prepared using ImageJ. Dot plots,
1266 correlation plots, and heat maps were created on R Studio. Flowcharts were created on
1267 and exported from BioRender.com (SD235B8ORF, KW235KT7TM, RZ235KTA0S).
1268 Final figures were organized and created using Adobe Illustrator CC.

1269

1270 **Statistics analysis**

1271 Data are expressed as mean \pm s.e.m, except the clinical analysis which is shown
1272 as a box and whisker plot showing the minimum, median, and maximum scores. A
1273 minimum of three biological replicates were used for all experiments, where separate
1274 HEK cell transfections, iPSC dox-inductions, mouse neuron cultures, or littermates are
1275 considered as individual replicates. All statistical analysis was done on GraphPad Prism
1276 7. All comparisons were assumed to be parametric, except for the clinical score
1277 analyses. ROUT's outlier test was used to identify possible outliers, with a Q value of
1278 0.1 %. For statistical analysis unpaired t-test, or One-Way ANOVA and Two-Way
1279 ANOVA with *post hoc* Holm-Sidak tests were used to compare all experimental
1280 conditions to the control condition. All unpaired t-tests were two-sided, except for the
1281 one-sided t-test used for identification of BiLD2 prey proteins. Clinical scores were
1282 assumed to be non-parametric and the Kruskal-Wallis H test with post hoc Dunn's test
1283 was used to compare all groups to each other. Any variation from the described
1284 statistical analyses is described and explained in the figure legends. The p-values are
1285 defined in the figure legends and $p < 0.05$ are considered statistically significant.

1286

1287 **Data availability**

1288 Mass spectrometry datasets consisting of raw files and results files with statistical
1289 analysis to identify PPI networks or significant DEPs will be deposited into
1290 ProteomeXchange through the Proteomics Identification Database. Individual PPI
1291 networks and shared ASD-risk gene PPI network map protein lists and enriched
1292 pathways can be found in Supplementary Tables 1-9. The Mouse_Human_Reactome
1293 and Mouse_GO_ALL_no_GO_jea gene sets used for overrepresentation and gene set
1294 enrichment analyses were downloaded on 13 August 2021 from
1295 http://download.baderlab.org/EM_Genesets/¹⁴⁶. RNA sequencing raw sequence files
1296 and results files with statistical analysis to identify significant DEGs will be deposited

1297 into the Gene Expression Omnibus. ASD proband variant information and clinical
1298 scores are available through the MSSNG database (research.mss.ng)¹² and the
1299 associated Metabase (data-explorer.mss.ng), respectively.

1300
1301

1302 **References**

- 1303 1. Ofner, M. *et al.* *Autism Spectrum Disorder among Children and Youth in Canada*
1304 *2018.* (2018).
- 1305 2. Gaugler, T. *et al.* Most genetic risk for autism resides with common variation. *Nat.*
1306 *Genet.* **46**, 881–885 (2014).
- 1307 3. Iossifov, I. *et al.* The contribution of de novo coding mutations to autism spectrum
1308 disorder. *Nature* **515**, 216–221 (2014).
- 1309 4. Robinson, E. B. *et al.* Genetic risk for autism spectrum disorders and
1310 neuropsychiatric variation in the general population. *Nat. Genet.* **48**, 552–555
1311 (2016).
- 1312 5. Weiner, D. J. *et al.* Polygenic transmission disequilibrium confirms that common
1313 and rare variation act additively to create risk for autism spectrum disorders. *Nat.*
1314 *Genet.* **49**, 978–985 (2017).
- 1315 6. Glessner, J. T. *et al.* Autism genome-wide copy number variation reveals ubiquitin
1316 and neuronal genes. *Nature* **459**, 569–573 (2009).
- 1317 7. Iossifov, I. *et al.* De Novo Gene Disruptions in Children on the Autistic Spectrum.
1318 *Neuron* **74**, 285–299 (2012).
- 1319 8. Neale, B. M. *et al.* Patterns and rates of exonic de novo mutations in autism
1320 spectrum disorders. *Nature* **485**, 242–245 (2012).
- 1321 9. O’Roak, B. J. *et al.* Sporadic autism exomes reveal a highly interconnected
1322 protein network of de novo mutations. *Nature* **485**, 246–250 (2012).
- 1323 10. Sanders, S. J. *et al.* De novo mutations revealed by whole-exome sequencing are
1324 strongly associated with autism. *Nature* **485**, 1–6 (2012).
- 1325 11. Sanders, S. J. *et al.* Insights into Autism Spectrum Disorder Genomic Architecture
1326 and Biology from 71 Risk Loci. *Neuron* **87**, 1215–1233 (2015).
- 1327 12. Yuen, R. K. C. *et al.* Whole genome sequencing resource identifies 18 new
1328 candidate genes for autism spectrum disorder. *Nat. Neurosci.* **20**, 602–611
1329 (2017).
- 1330 13. Feliciano, P. *et al.* Exome sequencing of 457 autism families recruited online
1331 provides evidence for novel ASD genes. *Genomic Med.* **4**,
1332 <https://doi.org/10.1038/s41525-019-0093-8> (2019).
- 1333 14. Ruzzo, E. K. *et al.* Inherited and De Novo Genetic Risk for Autism Article Inherited
1334 and De Novo Genetic Risk for Autism Impacts Shared Networks. *Cell* **178**, 850–
1335 866 (2019).
- 1336 15. Satterstrom, F. K. *et al.* Large-Scale Exome Sequencing Study Implicates Both
1337 Developmental and Functional Changes in the Neurobiology of Autism. *Cell* **180**,
1338 568-584.e23 (2020).
- 1339 16. Wilfert, A. B. *et al.* Recent ultra-rare inherited variants implicate new autism
1340 candidate risk genes. *Nat. Genet.* **53**, 1125–1134 (2021).
- 1341 17. Parikshak, N. N. *et al.* Integrative functional genomic analyses implicate specific
1342 molecular pathways and circuits in autism. *Cell* **155**, 1008 (2013).

- 1343 18. Willsey, A. J. *et al.* Coexpression networks implicate human midfetal deep cortical
1344 projection neurons in the pathogenesis of autism. *Cell* **155**, 997 (2013).
- 1345 19. Ramaswami, G. *et al.* Integrative genomics identifies a convergent molecular
1346 subtype that links epigenomic with transcriptomic differences in autism. *Nat.*
1347 *Commun.* **11**, 1–14 (2020).
- 1348 20. Jin, X. *et al.* In vivo Perturb-Seq reveals neuronal and glial abnormalities
1349 associated with autism risk genes. *Science (80-.)*. **370**, eaaz6063 (2020).
- 1350 21. Cederquist, G. Y. *et al.* A Multiplex Human Pluripotent Stem Cell Platform Defines
1351 Molecular and Functional Subclasses of Autism-Related Genes. *Cell Stem Cell*
1352 **27**, 35-49.e6 (2020).
- 1353 22. Willsey, H. R. *et al.* Parallel in vivo analysis of large-effect autism genes
1354 implicates cortical neurogenesis and estrogen in risk and resilience. *Neuron* **109**,
1355 788–804 (2021).
- 1356 23. O’Roak, B. J. *et al.* Multiplex targeted sequencing identifies recurrently mutated
1357 genes in autism spectrum disorders. *Science (80-.)*. **338**, 1619–1622 (2012).
- 1358 24. Voineagu, I. *et al.* Transcriptomic analysis of autistic brain reveals convergent
1359 molecular pathology. *Nature* **474**, 380–384 (2011).
- 1360 25. Velmeshev, D. *et al.* Single-cell genomics identifies cell type-specific molecular
1361 changes in autism. *Science (80-.)*. **364**, 685–689 (2019).
- 1362 26. Chang, J., Gilman, S. R., Chiang, A. H., Sanders, S. J. & Vitkup, D. Genotype to
1363 phenotype relationships in autism spectrum disorders. *Nat. Neurosci.* **18**, 191–
1364 198 (2015).
- 1365 27. De Rubeis, S. *et al.* Synaptic, transcriptional and chromatin genes disrupted in
1366 autism. *Nature* **515**, 209–215 (2014).
- 1367 28. Kuzmanov, U. & Emili, A. Protein-protein interaction networks: Probing disease
1368 mechanisms using model systems. *Genome Med.* **5**, 1–12 (2013).
- 1369 29. Murtaza, N., Uy, J. & Singh, K. K. Emerging proteomic approaches to identify the
1370 underlying pathophysiology of neurodevelopmental and neurodegenerative
1371 disorders. *Mol. Autism* **11**, 27 (2020).
- 1372 30. Chen, S. *et al.* De novo missense variants disrupting protein-protein interactions
1373 affect risk for autism through gene co-expression and protein networks in
1374 neuronal cell types. *Mol. Autism* **11**, 1–16 (2020).
- 1375 31. Corominas, R. *et al.* Protein interaction network of alternatively spliced isoforms
1376 from brain links genetic risk factors for autism. *Nat. Commun.* **5**, 1–12 (2014).
- 1377 32. Sakai, Y. *et al.* Protein interactome reveals converging molecular pathways
1378 among autism disorders. *Sci. Transl. Med.* **3**, 86ra49 (2011).
- 1379 33. Lage, K. Protein-protein interactions and genetic diseases: The interactome.
1380 *Biochim. Biophys. Acta - Mol. Basis Dis.* **1842**, 1971–1980 (2014).
- 1381 34. Richards, A. L., Eckhardt, M. & Krogan, N. J. Mass spectrometry-based protein-
1382 protein interaction networks for the study of human diseases. *Mol. Syst. Biol.* **17**,
1383 1–18 (2021).
- 1384 35. Casanova, E. L. *et al.* Autism risk genes are evolutionarily ancient and maintain a
1385 unique feature landscape that echoes their function. *Autism Res.* **12**, 860–869
1386 (2019).
- 1387 36. Uezu, A. *et al.* Identification of an elaborate complex mediating postsynaptic
1388 inhibition. *Science (80-.)*. **353**, 1123–1129 (2016).

- 1389 37. Spence, E. F. *et al.* In vivo proximity proteomics of nascent synapses reveals a
1390 novel regulator of cytoskeleton-mediated synaptic maturation. *Nat. Commun.* **10**,
1391 1–16 (2019).
- 1392 38. Loh, K. H. *et al.* Proteomic Analysis of Unbounded Cellular Compartments :
1393 Synaptic Clefts Resource Proteomic Analysis of Unbounded Cellular
1394 Compartments : Synaptic Clefts. *Cell* **166**, 1295-1307.e21 (2016).
- 1395 39. Hamdan, H. *et al.* Mapping axon initial segment structure and function by
1396 multiplexed proximity biotinylation. *Nat. Commun.* **11**, (2020).
- 1397 40. Go, C. D. *et al.* A proximity-dependent biotinylation map of a human cell. *Nature*
1398 **595**, (2021).
- 1399 41. Markmiller, S. *et al.* Context-Dependent and Disease-Specific Diversity in Protein
1400 Interactions within Stress Granules. *Cell* **172**, 590–604 (2018).
- 1401 42. Hung, V. *et al.* Proteomic mapping of cytosol-facing outer mitochondrial and ER
1402 membranes in living human cells by proximity biotinylation. *Elife* **6**, e24463
1403 (2017).
- 1404 43. Nowakowski, T. J. *et al.* Spatiotemporal gene expression trajectories reveal
1405 developmental hierarchies of the human cortex. *Science (80-.)*. **358**, 1318–1323
1406 (2017).
- 1407 44. Barres, B. A. The Mystery and Magic of Glia: A Perspective on Their Roles in
1408 Health and Disease. *Neuron* **60**, 430–440 (2008).
- 1409 45. Stogsdill, J. A. & Eroglu, C. The interplay between neurons and glia in synapse
1410 development and plasticity. *Curr. Opin. Neurobiol.* **42**, 1–8 (2017).
- 1411 46. Wilton, D. K., Dissing-Olesen, L. & Stevens, B. Neuron-Glia Signaling in Synapse
1412 Elimination. *Annu. Rev. Neurosci.* **42**, 107–127 (2019).
- 1413 47. Snel, B., Lehmann, G., Bork, P. & Huynen, M. A. String: A web-server to retrieve
1414 and display the repeatedly occurring neighbourhood of a gene. *Nucleic Acids*
1415 *Res.* **28**, 3442–3444 (2000).
- 1416 48. Trost, B. *et al.* Genome-wide detection of tandem DNA repeats that are expanded
1417 in autism. *Nature* **586**, 80–86 (2020).
- 1418 49. Cox, J. & Mann, M. MaxQuant enables high peptide identification rates,
1419 individualized p.p.b.-range mass accuracies and proteome-wide protein
1420 quantification. *Nat. Biotechnol.* **26**, 1367–1372 (2008).
- 1421 50. Fernández, E. *et al.* Targeted tandem affinity purification of PSD-95 recovers core
1422 postsynaptic complexes and schizophrenia susceptibility proteins. *Mol. Syst. Biol.*
1423 **5**, (2009).
- 1424 51. Fazal, F. M. *et al.* Atlas of Subcellular RNA Localization Revealed by APEX-Seq.
1425 *Cell* **178**, 473-490.e26 (2019).
- 1426 52. Bülow, P., Zlatic, S. A., Wenner, P. A., Bassell, G. J. & Faundez, V. FMRP
1427 attenuates activity dependent modifications in the mitochondrial proteome. *Mol.*
1428 *Brain* **14**, 1–11 (2021).
- 1429 53. Licznarski, P. *et al.* ATP Synthase c-Subunit Leak Causes Aberrant Cellular
1430 Metabolism in Fragile X Syndrome. *Cell* **182**, 1170–1185 (2020).
- 1431 54. Shulyakova, N., Andreatza, A. C., Mills, L. R. & Eubanks, J. H. Mitochondrial
1432 dysfunction in the pathogenesis of rett syndrome: Implications for mitochondria-
1433 targeted therapies. *Front. Cell. Neurosci.* **11**, 1–9 (2017).
- 1434 55. Rose, S. *et al.* Butyrate enhances mitochondrial function during oxidative stress in

- 1435 cell lines from boys with autism. *Transl. Psychiatry* **8**, (2018).
- 1436 56. Rose, S. *et al.* Oxidative stress induces mitochondrial dysfunction in a subset of
1437 autistic lymphoblastoid cell lines. *Transl. Psychiatry* **4**, 1–8 (2014).
- 1438 57. Shen, L., Feng, C., Zhang, K., Chen, Y. & Gao, Y. Proteomics Study of Peripheral
1439 Blood Mononuclear Cells (PBMCs) in Autistic Children. *Front. Cell. Neurosci.* **13**,
1440 1–16 (2019).
- 1441 58. Frye, R. E. Mitochondrial Dysfunction in Autism Spectrum Disorder : Unique
1442 Abnormalities and Targeted Treatments. *Semin. Pediatr. Neurol.* **35**, 100829
1443 (2020).
- 1444 59. Richter, M. *et al.* Altered TAOK2 activity causes autism-related
1445 neurodevelopmental and cognitive abnormalities through RhoA signaling. *Mol.*
1446 *Psychiatry* **24**, 1329–1350 (2019).
- 1447 60. Ultanir, S. K. K. *et al.* MST3 Kinase Phosphorylates TAO1/2 to Enable Myosin Va
1448 Function in Promoting Spine Synapse Development. *Neuron* **84**, 968–982 (2014).
- 1449 61. Calderon de Anda, F. *et al.* Autism spectrum disorder susceptibility gene TAOK2
1450 affects basal dendrite formation in the neocortex. *Nat. Neurosci.* **15**, 1022–1031
1451 (2012).
- 1452 62. Yadav, S. *et al.* TAOK2 Kinase Mediates PSD95 Stability and Dendritic Spine
1453 Maturation through Septin7 Phosphorylation. *Neuron* **93**, 1–15 (2017).
- 1454 63. Da Costa, R. M., Karmirian, K. & Rehen, S. K. Deformation of mitochondrial
1455 cristae in human neural progenitor cells exposed to valproic acid. *An. Acad. Bras.*
1456 *Cienc.* **90**, 2223–2232 (2018).
- 1457 64. John, G. B. *et al.* The Mitochondrial Inner Membrane Protein Mitofilin Controls
1458 Cristae Morphology. *Mol Biol Cell* **16**, 1543–1554 (2005).
- 1459 65. Schmidt, O., Pfanner, N. & Meisinger, C. Mitochondrial protein import: From
1460 proteomics to functional mechanisms. *Nat. Rev. Mol. Cell Biol.* **11**, 655–667
1461 (2010).
- 1462 66. Yang, W. *et al.* Rheb mediates neuronal-activity-induced mitochondrial energetics
1463 through mTORC1-independent PDH activation. *Dev. Cell* **56**, 811-825.e6 (2021).
- 1464 67. Hart, T. *et al.* High-Resolution CRISPR Screens Reveal Fitness Genes and
1465 Genotype-Specific Cancer Liabilities. *Cell* **163**, 1515–1526 (2015).
- 1466 68. Richardson, C. D., Ray, G. J., DeWitt, M. A., Curie, G. L. & Corn, J. E. Enhancing
1467 homology-directed genome editing by catalytically active and inactive CRISPR-
1468 Cas9 using asymmetric donor DNA. *Nat. Biotechnol.* **34**, 339–344 (2016).
- 1469 69. Ruggiero, A., Katsenelson, M. & Slutsky, I. Trends in Mitochondria : new players
1470 in homeostatic regulation of firing rate set points. *Trends Neurosci.* **44**, 605–618
1471 (2021).
- 1472 70. Deneault, E. *et al.* Complete Disruption of Autism-Susceptibility Genes by Gene
1473 Editing Predominantly Reduces Functional Connectivity of Isogenic Human
1474 Neurons. *Stem Cell Reports* **11**, 1211–1225 (2018).
- 1475 71. Deneault, E. *et al.* CNTN5-/+or EHMT2-/+human iPSC-derived neurons from
1476 individuals with autism develop hyperactive neuronal networks. *Elife* **8**, 1–26
1477 (2019).
- 1478 72. Zhang, Y. *et al.* Rapid single-step induction of functional neurons from human
1479 pluripotent stem cells. *Neuron* **78**, 785–798 (2013).
- 1480 73. Geisheker, M. R. *et al.* Hotspots of missense mutation identify

- 1481 neurodevelopmental disorder genes and functional domains. *Nat. Neurosci.* **20**,
1482 1043–1051 (2017).
- 1483 74. de Ligt, J. *et al.* Diagnostic Exome Sequencing in Persons with Severe Intellectual
1484 Disability. *N. Engl. J. Med.* **367**, 1921–1929 (2012).
- 1485 75. Pick, J. E. & Ziff, E. B. Regulation of AMPA receptor trafficking and exit from the
1486 endoplasmic reticulum. *Mol. Cell. Neurosci.* **91**, 3–9 (2018).
- 1487 76. Schwenk, J. *et al.* An ER Assembly Line of AMPA-Receptors Controls Excitatory
1488 Neurotransmission and Its Plasticity. *Neuron* **104**, 680-692.e9 (2019).
- 1489 77. Shang, L. *et al.* De novo missense variants in PPP2R5D are associated with
1490 intellectual disability, macrocephaly, hypotonia, and autism. *Neurogenetics* **17**,
1491 43–49 (2016).
- 1492 78. Houge, G. *et al.* B56δ-related protein phosphatase 2A dysfunction identified in
1493 patients with intellectual disability. *J. Clin. Invest.* **125**, 3051–3062 (2015).
- 1494 79. Papke, C. M. *et al.* A disorder-related variant (E420K) of a PP2A-regulatory
1495 subunit (PPP2R5D) causes constitutively active AKT-mTOR signaling and
1496 uncoordinated cell growth. *J. Biol. Chem.* **296**, 100313 (2021).
- 1497 80. Xu, Z. X. *et al.* Elevated protein synthesis in microglia causes autism-like synaptic
1498 and behavioral aberrations. *Nat. Commun.* **11**, (2020).
- 1499 81. Tang, G. *et al.* Loss of mTOR-Dependent Macroautophagy Causes Autistic-like
1500 Synaptic Pruning Deficits. *Neuron* **83**, 1131–1143 (2014).
- 1501 82. Flaherty, E. *et al.* Neuronal impact of patient-specific aberrant NRXN1α splicing.
1502 *Nat. Genet.* **51**, 1679–1690 (2019).
- 1503 83. Li, J. *et al.* Identification of Human Neuronal Protein Complexes Reveals
1504 Biochemical Activities and Convergent Mechanisms of Action in Autism Spectrum
1505 Disorders. *Cell Syst.* **1**, 361–374 (2015).
- 1506 84. May, D. G., Scott, K. L., Campos, A. R. & Roux, K. J. Comparative Application of
1507 BiOLD and TurboOLD for Protein-Proximity Biotinylation. *Cells* **9**, (2020).
- 1508 85. Minde, D. P., Ramakrishna, M. & Lilley, K. S. Biotin proximity tagging favours
1509 unfolded proteins and enables the study of intrinsically disordered regions.
1510 *Commun. Biol.* **3**, 1–13 (2020).
- 1511 86. Niinae, T., Imami, K., Sugiyama, N. & Ishihama, Y. Proximity Labeling-assisted
1512 Identification of Endogenous Kinase Substrates. *BioRxiv* (2020).
1513 doi:10.1101/2020.06.09.143370
- 1514 87. Branon, T. C. *et al.* Efficient proximity labeling in living cells and organisms with
1515 TurboOLD. *Nat. Biotechnol.* **36**, 880–898 (2018).
- 1516 88. Brown, E. A. *et al.* Clustering the autisms using glutamate synapse protein
1517 interaction networks from cortical and hippocampal tissue of seven mouse
1518 models. *Mol. Autism* **9**, 1–16 (2018).
- 1519 89. Gazestani, V. H. *et al.* A perturbed gene network containing PI3K-AKT, RAS-ERK
1520 and WNT-B-catenin pathways in leukocytes is linked to ASD genetics and
1521 symptom severity. *Nat. Neurosci.* **22**, (2019).
- 1522 90. Iwata, R., Casimir, P. & Vanderhaeghen, P. Mitochondrial dynamics in postmitotic
1523 cells regulate neurogenesis. *Science (80-.)*. **862**, 858–862 (2020).
- 1524 91. Rossignol, D. A. & Frye, R. E. Mitochondrial dysfunction in autism spectrum
1525 disorders: A systematic review and meta-analysis. *Mol. Psychiatry* **17**, 290–314
1526 (2012).

- 1527 92. Frye, R. E. *et al.* Redox metabolism abnormalities in autistic children associated
1528 with mitochondrial disease. *Transl. Psychiatry* **3**, 1–12 (2013).
- 1529 93. Frye, R. E. & Rossignol, D. A. Mitochondrial dysfunction can connect the diverse
1530 medical symptoms associated with autism spectrum disorders. *Pediatr. Res.* **69**,
1531 41–47 (2011).
- 1532 94. Anitha, A. *et al.* Brain region-specific altered expression and association of
1533 mitochondria-related genes in autism. *Mol. Autism* **3**, 1–12 (2012).
- 1534 95. Wang, Y., Picard, M. & Gu, Z. Genetic Evidence for Elevated Pathogenicity of
1535 Mitochondrial DNA Heteroplasmy in Autism Spectrum Disorder. *PLoS Genet.* **12**,
1536 1–24 (2016).
- 1537 96. Kurochkin, I. *et al.* Metabolome signature of autism in the human prefrontal
1538 cortex. *Commun. Biol.* **2**, 1–10 (2019).
- 1539 97. Yardeni, T., Cristancho, A. G., Mccoy, A. J., Schaefer, P. M. & Mcmanus, M. J. An
1540 mtDNA mutant mouse demonstrates that mitochondrial deficiency can result in
1541 autism endophenotypes. *Proc. Natl. Acad. Sci. U. S. A.* **118**, 1–11 (2021).
- 1542 98. Shen, M. *et al.* Reduced mitochondrial fusion and Huntingtin levels contribute to
1543 impaired dendritic maturation and behavioral deficits in Fmr1-mutant mice. *Nat.*
1544 *Neurosci.* **22**, 386–400 (2019).
- 1545 99. Ebrahimi-fakhari, D. *et al.* Impaired Mitochondrial Dynamics and Mitophagy in
1546 Neuronal Models of Tuberous Sclerosis Complex. *Cell Rep.* **17**, 1053–1070
1547 (2016).
- 1548 100. Kanellopoulos, A. K. *et al.* Aralar Sequesters GABA into Hyperactive Article Aralar
1549 Sequesters GABA into Hyperactive Mitochondria , Causing Social Behavior
1550 Deficits. *Cell* **180**, 1178-1197.e20 (2020).
- 1551 101. Menzies, C. *et al.* Distinct basal metabolism in three mouse models of
1552 neurodevelopmental disorders. *eNeuro* **8**, 1–14 (2021).
- 1553 102. Li, J. *et al.* Mitochondrial deficits in human iPSC-derived neurons from patients
1554 with 22q11.2 deletion syndrome and schizophrenia. *Transl. Psychiatry* **9**, (2019).
- 1555 103. Jagtap, S. *et al.* Aberrant mitochondrial function in patient-derived neural cells
1556 from CDKL5 deficiency disorder and Rett syndrome. *Hum. Mol. Genet.* **28**, 3625–
1557 3636 (2019).
- 1558 104. Fernandez, A. *et al.* Mitochondrial Dysfunction Leads to Cortical Under-
1559 Connectivity and Cognitive Impairment 22q11. *Neuron* **102**, 1127-1142.e3 (2019).
- 1560 105. Madison, J. M. *et al.* Regulation of purine metabolism connects KCTD13 to a
1561 metabolic disorder with autistic features. *iScience* **24**, 101935 (2021).
- 1562 106. Heinemann-Yerushalmi, L. *et al.* BCKDK regulates the TCA cycle through PDC in
1563 the absence of PDK family during embryonic development. *Dev. Cell* **56**, 1182-
1564 1194.e6 (2021).
- 1565 107. Namba, T., Nardelli, J., Gressens, P. & Huttner, W. B. Perspective Metabolic
1566 Regulation of Neocortical Expansion in Development and Evolution. *Neuron* **109**,
1567 408–419 (2021).
- 1568 108. Fendt, S. M. & Verstreken, P. Neurons eat glutamate to stay alive. *J. Cell Biol.*
1569 **216**, 863–865 (2017).
- 1570 109. Divakaruni, S. S. *et al.* Long-Term Potentiation Requires a Rapid Burst of
1571 Dendritic Mitochondrial Fission during Induction. *Neuron* **100**, 1–16 (2018).
- 1572 110. Chen, S. *et al.* An interactome perturbation framework prioritizes damaging

- 1573 missense mutations for developmental disorders. *Nat. Genet.* **50**, 1032–1040
1574 (2018).
- 1575 111. Chou, C. *et al.* TDP-43 pathology disrupts nuclear pore complexes and
1576 nucleocytoplasmic transport in ALS/FTD. *Nat. Neurosci.* **21**, (2018).
- 1577 112. Tracy, T. E. *et al.* Tau interactome mapping reveals dynamic processes in
1578 synapses and mitochondria associated with neurodegenerative disease. *bioRxiv*
1579 <https://doi.org/10.1101/2021.06.17.448349> (2021).
- 1580 113. Pintacuda, G. *et al.* Interaction studies of risk proteins in human induced neurons
1581 reveal convergent biology and novel mechanisms underlying autism spectrum
1582 disorders. *medRxiv* <https://doi.org/10.1101/2021.10.07.21264575> (2021).
- 1583 114. Meili, F. *et al.* Multi-parametric analysis of 57 SYNGAP1 variants reveal impacts
1584 on GTPase signaling, localization, and protein stability. *Am. J. Hum. Genet.* **108**,
1585 148–162 (2021).
- 1586 115. Post, K. L. *et al.* Multi-model functionalization of disease-associated PTEN
1587 missense mutations identifies multiple molecular mechanisms underlying protein
1588 dysfunction. *Nat. Commun.* **11**, (2020).
- 1589 116. Koire, A. *et al.* A method to delineate de novo missense variants across pathways
1590 prioritizes genes linked to autism. *Sci. Transl. Med.* **13**, eabc1739 (2021).
- 1591 117. Wu, Y., Li, R., Sun, S., Weile, J. & Roth, F. P. Improved pathogenicity prediction
1592 for rare human missense variants. *Am. J. Hum. Genet.* **108**, 1891–1906 (2021).
- 1593 118. Lek, M. *et al.* Analysis of protein-coding genetic variation in 60,706 humans.
1594 *Nature* **536**, 285–291 (2016).
- 1595 119. Adzhubei, I. A. *et al.* A method and server for predicting damaging missense
1596 mutations. *Nat. Methods* **7**, 248–249 (2010).
- 1597 120. Nathanson, J. L., Yanagawa, Y., Obata, K. & Callaway, E. M. Preferential labeling
1598 of inhibitory and excitatory cortical neurons by endogenous tropism of adeno-
1599 associated virus and lentivirus vectors. *nsc. NSC* **161**, 441–450 (2009).
- 1600 121. Barger, C. J., Branick, C., Chee, L. & Karpf, A. R. Pan-cancer analyses reveal
1601 genomic features of FOXM1 overexpression in cancer. *Cancers (Basel)*. **11**, 251
1602 (2019).
- 1603 122. Johannessen, C. M. *et al.* COT drives resistance to RAF inhibition through MAP
1604 kinase pathway reactivation. *Nature* **468**, 968–972 (2010).
- 1605 123. Kim, E. *et al.* Systematic functional interrogation of rare cancer variants identifies
1606 oncogenic alleles. *Cancer Discov.* **6**, 714–726 (2016).
- 1607 124. Braun, J. E., Huntzinger, E., Fauser, M. & Izaurralde, E. GW182 proteins directly
1608 recruit cytoplasmic deadenylase complexes to miRNA targets. *Mol. Cell* **44**, 120–
1609 133 (2011).
- 1610 125. Butko, M. T. *et al.* Fluorescent and photo-oxidizing TimeSTAMP tags track protein
1611 fates in light and electron microscopy. *Nat. Neurosci.* **15**, 1742–1751 (2012).
- 1612 126. Ohno, H. *et al.* Localization of p0071-interacting proteins, plakophilin-related
1613 armadillo-repeat protein-interacting protein (PAPIN) and ERBIN, in epithelial cells.
1614 *Oncogene* **21**, 7042–7049 (2002).
- 1615 127. Wang, S., Tukachinsky, H., Romano, F. B. & Rapoport, T. A. Cooperation of the
1616 ER-shaping proteins atlastin, lunapark, and reticulons to generate a tubular
1617 membrane network. *Elife* **5**, 1–29 (2016).
- 1618 128. Hiday, A. C. *et al.* Mechanisms and Consequences of Dopamine Depletion-

- 1619 Induced Attenuation of the Spinophilin/Neurofilament Medium Interaction. *Neural*
1620 *Plast.* **2017**, (2017).
- 1621 129. Seeling, J. M. *et al.* Regulation of β -catenin signaling by the B56 subunit of protein
1622 phosphatase 2A. *Science (80-.)*. **283**, 2089–2091 (1999).
- 1623 130. Urano, J. *et al.* Point mutations in TOR confer Rheb-independent growth in fission
1624 yeast and nutrient-independent mammalian TOR signaling in mammalian cells.
1625 *Proc. Natl. Acad. Sci. U. S. A.* **104**, 3514–3519 (2007).
- 1626 131. Solowska, J. M., Garbern, J. Y. & Baas, P. W. Evaluation of loss of function as an
1627 explanation for SPG4-based hereditary spastic paraplegia. *Hum. Mol. Genet.* **19**,
1628 2767–2779 (2010).
- 1629 132. Braganza, A. *et al.* UBE3B is a calmodulin-regulated, mitochondrion-associated
1630 E3 ubiquitin ligase. *J. Biol. Chem.* **292**, 2470–2484 (2017).
- 1631 133. Sowa, M. E., Bennett, E. J., Gygi, S. P. & Harper, J. W. Defining the Human
1632 Deubiquitinating Enzyme Interaction Landscape. *Cell* **138**, 389–403 (2009).
- 1633 134. Cummins, J. M. & Vogelstein, B. HAUSP is required for p53 destabilization. *Cell*
1634 *Cycle* **3**, 689–692 (2004).
- 1635 135. Howarth, M., Takao, K., Hayashi, Y. & Ting, A. Y. Targeting quantum dots to
1636 surface proteins in living cells with biotin ligase. *Proc. Natl. Acad. Sci. U. S. A.*
1637 **102**, 7583–7588 (2005).
- 1638 136. Furlong, R. A., Narain, Y., Rankin, J., Wytenbach, A. & Rubinsztein, D. C. α -
1639 Synuclein overexpression promotes aggregation of mutant huntingtin. *Biochem. J.*
1640 **346**, 577–581 (2000).
- 1641 137. Małeckı, J., Ho, A. Y. Y., Moen, A., Dahl, H. A. & Falnes, P. Human METTL20 is a
1642 mitochondrial lysine methyltransferase that targets the β subunit of electron
1643 transfer flavoprotein (ETF β) and modulates its activity. *J. Biol. Chem.* **290**, 423–
1644 434 (2015).
- 1645 138. Alford, S. C., Ding, Y., Simmen, T. & Campbell, R. E. Dimerization-dependent
1646 green and yellow fluorescent proteins. *ACS Synth. Biol.* **1**, 569–575 (2012).
- 1647 139. Lu, G. *et al.* The myeloma drug lenalidomide promotes the cereblon-dependent
1648 destruction of ikaros proteins. *Science (80-.)*. **343**, 305–309 (2014).
- 1649 140. Hockemeyer, D. *et al.* A Drug-Inducible System for Direct Reprogramming of
1650 Human Somatic Cells to Pluripotency. *Cell Stem Cell* **3**, 346–353 (2008).
- 1651 141. Ran, F. A. *et al.* Genome engineering using the CRISPR-Cas9 system. *Nat.*
1652 *Protoc.* **8**, 2281–2308 (2013).
- 1653 142. Kapfhamer, D. *et al.* *Taok2* controls behavioral response to ethanol in mice.
1654 *Genes, Brain Behav.* **12**, 87–97 (2013).
- 1655 143. Yacoub, N. al, Romanowska, M., Haritonova, N. & Foerster, J. Optimized
1656 production and concentration of lentiviral vectors containing large inserts. *J. Gene*
1657 *Med.* **9**, 579–584 (2012).
- 1658 144. Bateman, A. *et al.* UniProt: The universal protein knowledgebase in 2021. *Nucleic*
1659 *Acids Res.* **49**, D480–D489 (2021).
- 1660 145. Raudvere, U. *et al.* G:Profiler: A web server for functional enrichment analysis and
1661 conversions of gene lists (2019 update). *Nucleic Acids Res.* **47**, W191–W198
1662 (2019).
- 1663 146. Merico, D., Isserlin, R., Stueker, O., Emili, A. & Bader, G. D. Enrichment map: A
1664 network-based method for gene-set enrichment visualization and interpretation.

- 1665 *PLoS One* **5**, e13984 (2010).
- 1666 147. Sharma, K. *et al.* Cell type- and brain region-resolved mouse brain proteome. *Nat.*
1667 *Neurosci.* **18**, 1819–1831 (2015).
- 1668 148. Kwan, V. *et al.* DIXDC1 Phosphorylation and Control of Dendritic Morphology Are
1669 Impaired by Rare Genetic Variants. *Cell Rep.* **17**, 1892–1904 (2016).
- 1670 149. Tyanova, S. *et al.* The Perseus computational platform for comprehensive
1671 analysis of (prote)omics data. *Nat. Methods* **13**, 731–740 (2016).
- 1672 150. Afgan, E. *et al.* The Galaxy platform for accessible, reproducible and collaborative
1673 biomedical analyses: 2018 update. *Nucleic Acids Res.* **46**, W537–W544 (2018).
- 1674 151. Subramanian, A. *et al.* Gene set enrichment analysis: A knowledge-based
1675 approach for interpreting genome-wide expression profiles. *Proc. Natl. Acad. Sci.*
1676 **102**, 15545–15550 (2005).
- 1677 152. Daly, M. J. *et al.* PGC-1 α -responsive genes involved in oxidative phosphorylation
1678 are coordinately downregulated in human diabetes. *Nat. Genet.* **34**, 267–273
1679 (2003).
- 1680 153. Shannon, P. *et al.* Cytoscape: A Software Environment for Integrated Models.
1681 *Genome Res.* **13**, 2498–2504 (2003).
- 1682 154. Bader, G. D., Isserlin, R., Merico, D. & Voisin, V. Enrichment Map - a Cytoscape
1683 app to visualize and explore OMICs pathway enrichment results. *F1000Research*
1684 **3**, 1–8 (2014).
- 1685 155. Kucera, M., Isserlin, R., Arkhangorodsky, A. & Bader, G. D. AutoAnnotate: A
1686 Cytoscape app for summarizing networks with semantic annotations [version 1;
1687 referees: 2 approved]. *F1000Research* **5**, 1–12 (2016).
- 1688
- 1689
- 1690
- 1691
- 1692
- 1693
- 1694
- 1695
- 1696
- 1697
- 1698
- 1699
- 1700
- 1701
- 1702
- 1703
- 1704
- 1705
- 1706
- 1707
- 1708
- 1709
- 1710

1711 **Acknowledgements**

1712 We thank C.I. and P.dG. for proof reading the manuscript. We also thank K.J.B.
1713 and M.B.F. for providing the NRXN1 cDNA. Flowcharts were created with
1714 BioRender.com (SD235B8ORF, KW235KT7TM, RZ235KTA0S). Work in the Singh Lab
1715 was supported by the Canadian Institute of Health Research (CIHR), the Ontario Brain
1716 Institute (OBI), the Network for European Funding for Neuroscience Research
1717 (NEURON ERA-NET), and the Donald K. Johnson Eye Institute at University Health
1718 Network.

1719

1720 **Author contributions**

1721 N.M. and K.K.S. conceived the project. N.M. and K.K.S. wrote the paper with
1722 input from A.A.C., B.T., W.E., B.T., and B.W.D. A.A.C and B.K.U created initial BiID2
1723 lentiviral construct backbone. N.M. generated all of subsequent DNA constructs and
1724 performed all experiments and data analysis unless otherwise specified. N.M and
1725 A.A.C. generated all lentiviruses. S.X. and Y.L. ran samples through the mass
1726 spectrometer and helped with data acquisition. C.O.B. performed all electrophysiology
1727 recordings. J.A.U, J.E.H., and N.P. helped perform western blots. D.P.M., S.H., B.S.,
1728 and F.C.dA. performed and analysed mitochondrial activity and content experiments in
1729 mouse cortical neurons. E.D., J.E, and S.W.S helped to create the human *TAOK2* KO
1730 and A135P iPSC lines. E.A. advised on clinical score analysis and G.D.B. advised on
1731 pathway analyses used in the project. K.S.S supervised the project.

1732

1733 **Competing interests**

1734 The authors declare no competing interests

1735

1736 **Materials & Correspondence**

1737 Correspondence and material requests to Karun K. Singh

1738

1739 **Supplementary Tables**

1740 Supplementary Table 1. BiID2 PPI networks of 41 ASD-risk genes and cellular
1741 compartment genes

1742 Supplementary Table 2. Comparison of BiID2 PPI networks identified in HEK293 cells
1743 and mouse cortical neurons

1744 Supplementary Table 3. Comparison of BiID2 PPI network enriched cellular
1745 components identified in HEK293 cells and mouse cortical neurons

1746 Supplementary Table 4. BiID2 PPI network enriched cellular components of
1747 compartment specific genes

1748 Supplementary Table 5. BiID2 PPI network enriched pathways of 41 ASD-risk genes

1749 Supplementary Table 6. 41 ASD-risk gene PPI network map enriched pathways

1750 Supplementary Table 7. Differentially expressed genes and proteins and dysregulated
1751 pathways in *Taok2* KO mouse cortices

1752 Supplementary Table 8. Comparison of BiID2 PPI networks between ASD-risk genes
1753 and their variants

1754 Supplementary Table 9. BiID2 PPI network enriched pathways of ASD-risk genes and
1755 their variants

1756 Supplementary Table 10. List of sources for 41 ASD-risk genes and cellular
1757 compartment genes

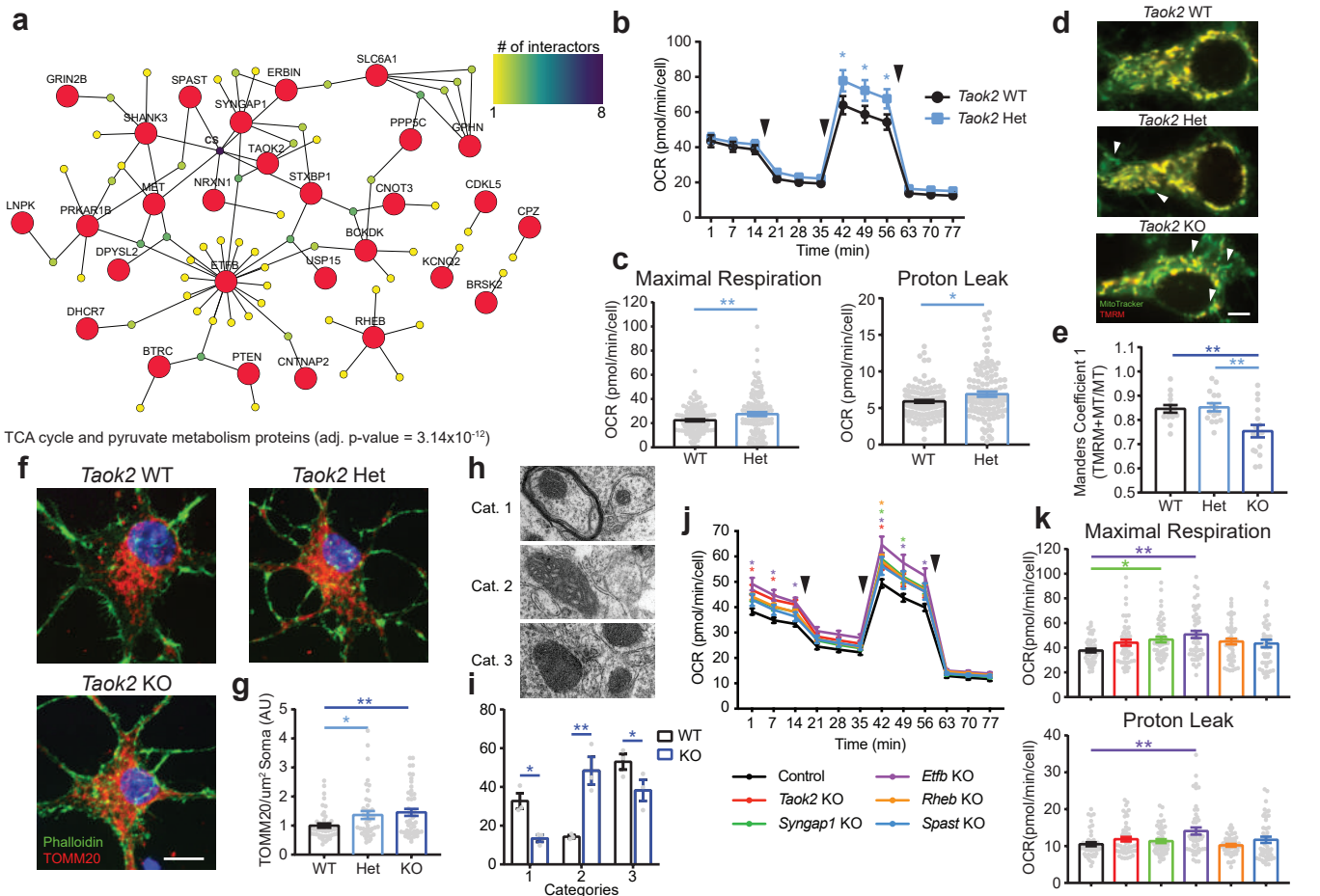


Figure 3. Regulation of cellular respiration and mitochondrial activity by ASD-risk genes

a, Network of TCA cycle and pyruvate metabolism proteins enriched in the shared ASD-risk gene PPI network map (g:Profiler, Benjamini-Hochberg FDR adj. $p < 0.05$). **b**, Loss of *Taok2* alters cellular respiration in DIV14 mouse cortical neurons (Two-Way ANOVA, $F(1, 336) = 18.22$, $p < 0.0001$ between genotypes, *post hoc* Holm-Sidak test; WT = 118 wells and Het = 122 wells from three separate cultures). **c**, Loss of *Taok2* increases maximal respiration (*left*) and proton leakage (*right*) in DIV14 mouse cortical neurons (ROUT outlier test, $Q = 0.1\%$; Two-tailed unpaired t-test, maximal respiration: $t = 3.015$, $df = 233$, $p = 0.0029$, proton leak: $t = 2.374$, $df = 225$, $p = 0.0184$; WT = 118 wells, Het = 122 wells from three separate cultures). **d**, Representative images of *Taok2* WT, Het, and KO neurons stained with MitoTrack (green) and TMRM (red). Arrows indicate Mitotracker-labeled mitochondria with no TMRM staining. Scale bar is 5 μm . **e**, *Taok2* Het and KO neurons have decreased number of active (TMRM) Mitotracker-labeled mitochondria (One-Way ANOVA, $F(2, 42) = 7.47$, $p = 0.0017$, *post hoc* Holm-Sidak test; WT = 14, Het = 15, KO = 15 neurons from 1-3 separate pups per genotype from one culture). **f**, Representative images of *Taok2* WT, Het, and KO neurons stained with TOMM20 (red) and Phalloidin (green). Scale bar 5 μm . **g**, *Taok2* Het and KO neurons have increased TOMM20 staining (One-Way ANOVA, $F(2, 132) = 4.633$, $p = 0.0111$; WT = 45, Het = 42, KO = 48 neurons from 1-4 separate pups per genotype from two cultures). **h**, Representative images of synaptic mitochondria morphological categories. **i**, *Taok2* KO neurons have increased proportion of category 2 mitochondria with enlarged cristae. (Two-way ANOVA, $F(1, 12) < 0.0001$, $p = 0.9998$ between genotypes, *post hoc* Holm-Sidak test. 19-25 images per animal and three animals per genotype). **j**, CRISPR/Cas9 KO of *Taok2*, *Syngap1*, *Etfb*, *Rheb*, and *Spast* differentially alters cellular respiration in DIV14 mouse cortical neurons (Two-Way ANOVA, $F(5, 280) = 3.492$, $p = 0.0044$, *post hoc* Holm-Sidak test; Control = 45 wells, *Taok2* KO = 51 wells, *Syngap1* KO = 50 wells, *Etfb* KO = 47 wells, *Rheb* KO = 48 wells, *Spast* KO = 45 wells from five separate cultures). **k**, Significant increases in maximal respiration (*top*) and proton leakage (*bottom*) show significant increase in *Syngap1* and *Etfb* KO neurons (ROUT outlier test, $Q = 0.1\%$; maximal respiration: One-Way ANOVA, $F(5, 280) = 2.927$, $p = 0.0136$, *post hoc* Holm-Sidak test, proton leak: One-Way ANOVA, $F(5, 277) = 4.138$, $p = 0.0012$, *post hoc* Holm-Sidak test). Mean \pm s.e.m. * $p < 0.05$, ** $p < 0.01$, *** $p < 0.001$.

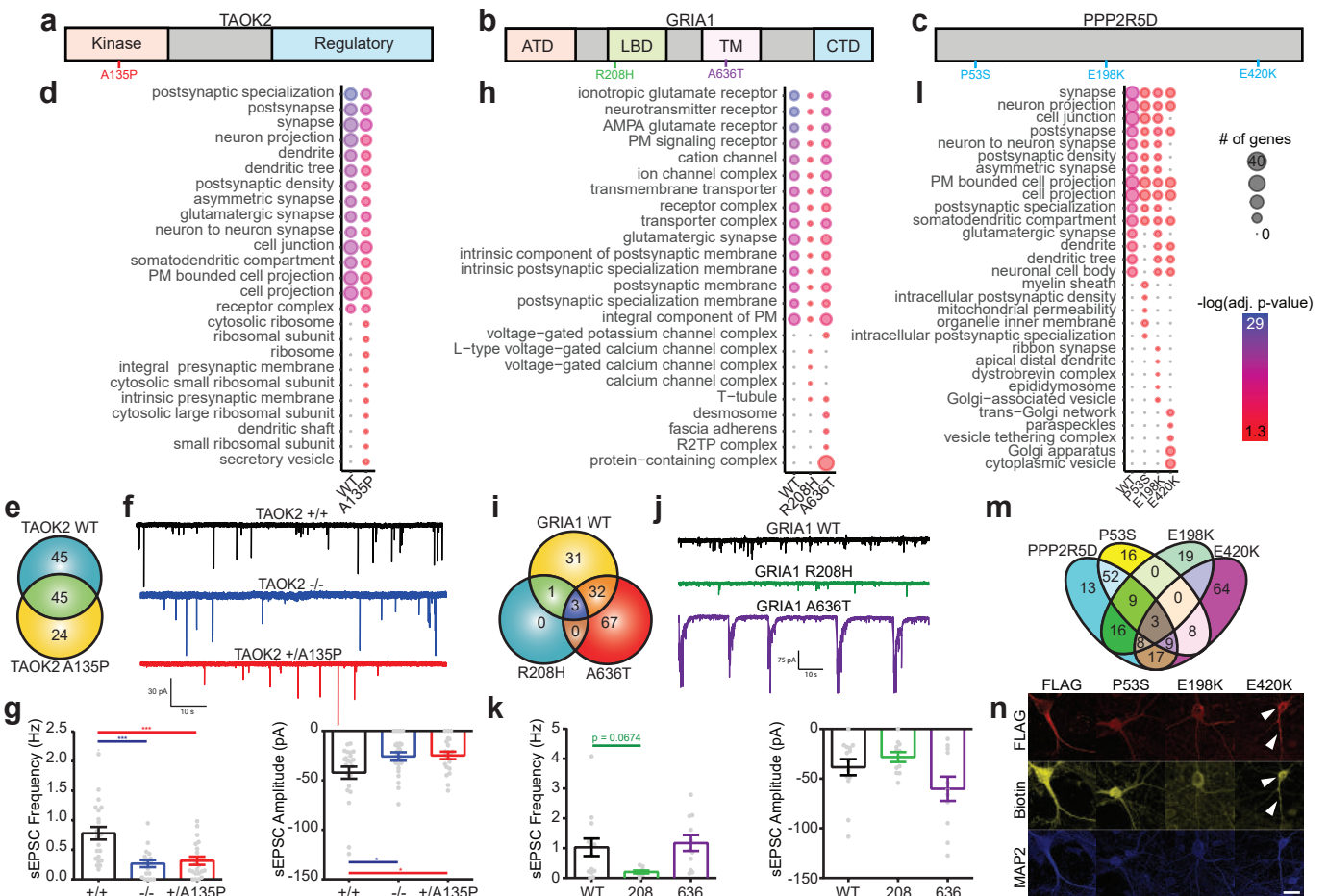


Figure 4. De novo missense variants alter the PPI networks of uncharacterized and established ASD-risk genes that correspond to functional deficits. **a-c**, Diagram of TAOK2, GRIA1, and PPP2R5D and location of *de novo* missense variants. ATD: amino-terminal domain, LBD: ligand-binding domain, TM: transmembrane domain, CTD: carboxy-terminal domain. **d**, Dot plot of top 15 cellular compartment gene sets and top 10 variant-specific gene sets identified in TAOK2 variants (g:Profiler, Benjamini-Hochberg FDR adj. $p < 0.05$). PM: plasma membrane. Size of dots indicate protein number and the color represents the significance. **e**, Venn diagram of PPI network proteins of TAOK2 WT and A135P. **f**, Representative traces of sEPSC recordings of DIV21 TAOK2 WT, KO, and A135P human iPSC-derived NG2 neurons. **g**, TAOK2 KO and A135P neurons show decreased sEPSC frequency (left) (ROUT Outlier Test, $Q = 0.1$); frequency: One-Way ANOVA, $F(2,57) = 11.63$, $p < 0.0001$, amplitude: One-Way ANOVA, $F(2,63) = 4.027$, $p = 0.0226$, *post hoc* Holm-Sidak test; WT = 23, KO = 22, and A135P = 21 neurons from three separate transductions). **h**, Dot plot of top 15 cellular compartment gene sets and top five variant-specific gene sets identified in GRIA1 variants (g:Profiler, Benjamini-Hochberg FDR adj. $p < 0.05$). **i**, Venn diagram of PPI network proteins of GRIA1 WT and variants. **j**, Representative traces of sEPSC recordings of mouse cortical neurons expressing GRIA1 or variants. **k**, R208H variant shows trend in decrease sEPSC frequency (left) and no change in amplitude (right). (ROUT Outlier Test, $Q = 0.1$); frequency: One-Way ANOVA, $F(2,31) = 3.506$, $p = 0.0424$, amplitude: One-Way ANOVA, $F(2,33) = 3.147$, $p = 0.0561$, *post hoc* Holm-Sidak test; WT = 14, R208H = 11, and A636T = 11 neurons from three separate infections). **l**, Dot plot of top 15 cellular compartment gene sets and top five variant-specific gene sets identified in PPP2R5D variants (g:Profiler, Benjamin Hochberg FDR adj. $p < 0.05$). **m**, Venn diagram of PPI network proteins of PPP2R5D WT and variants. **n**, Representative images of neurons infected with PPP2R5D WT and variants show mislocalization of E420K variant (white arrows). Scale bar is 25 μm. Mean ± s.e.m. * $p < 0.05$, ** $p < 0.01$, *** $p < 0.001$.

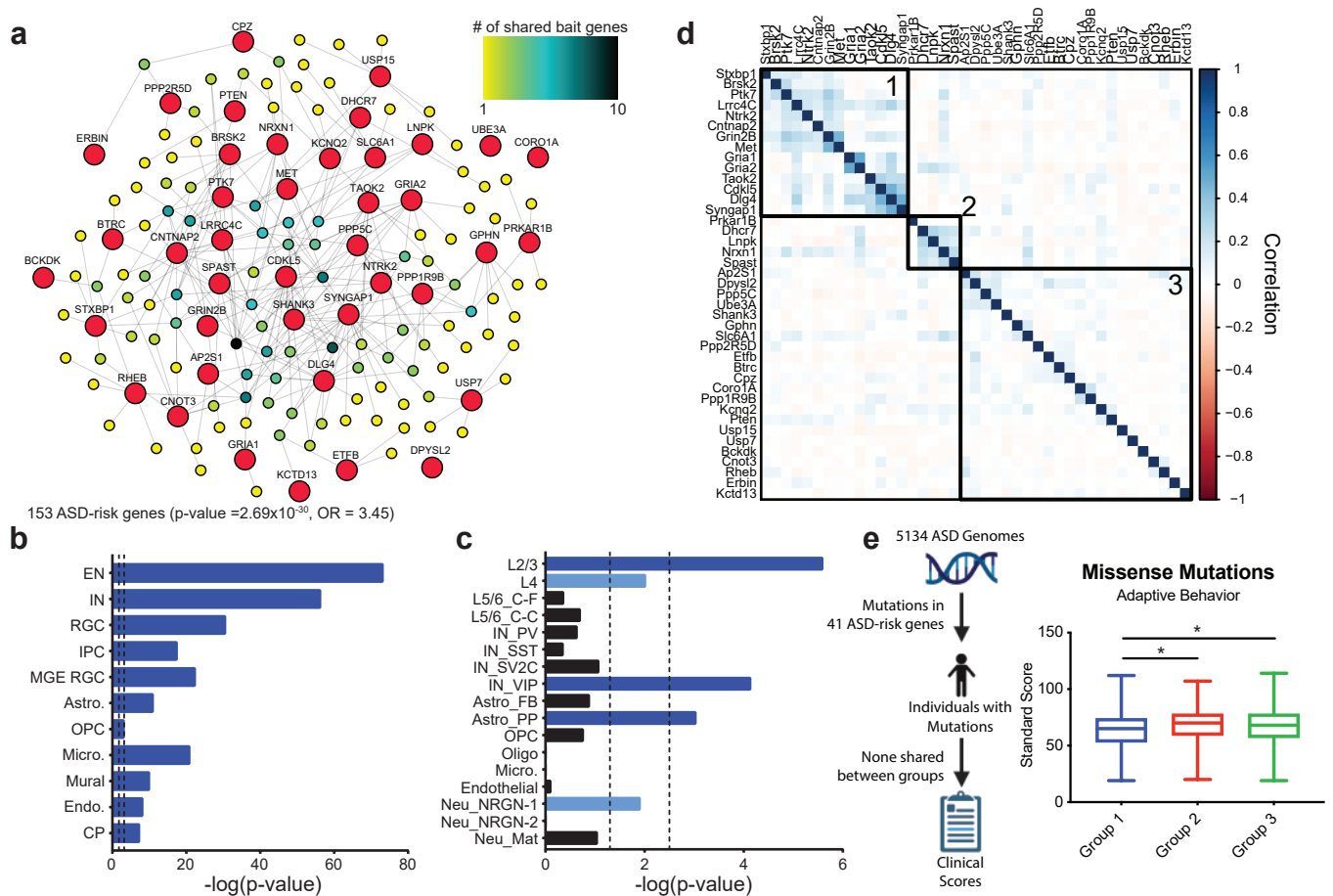
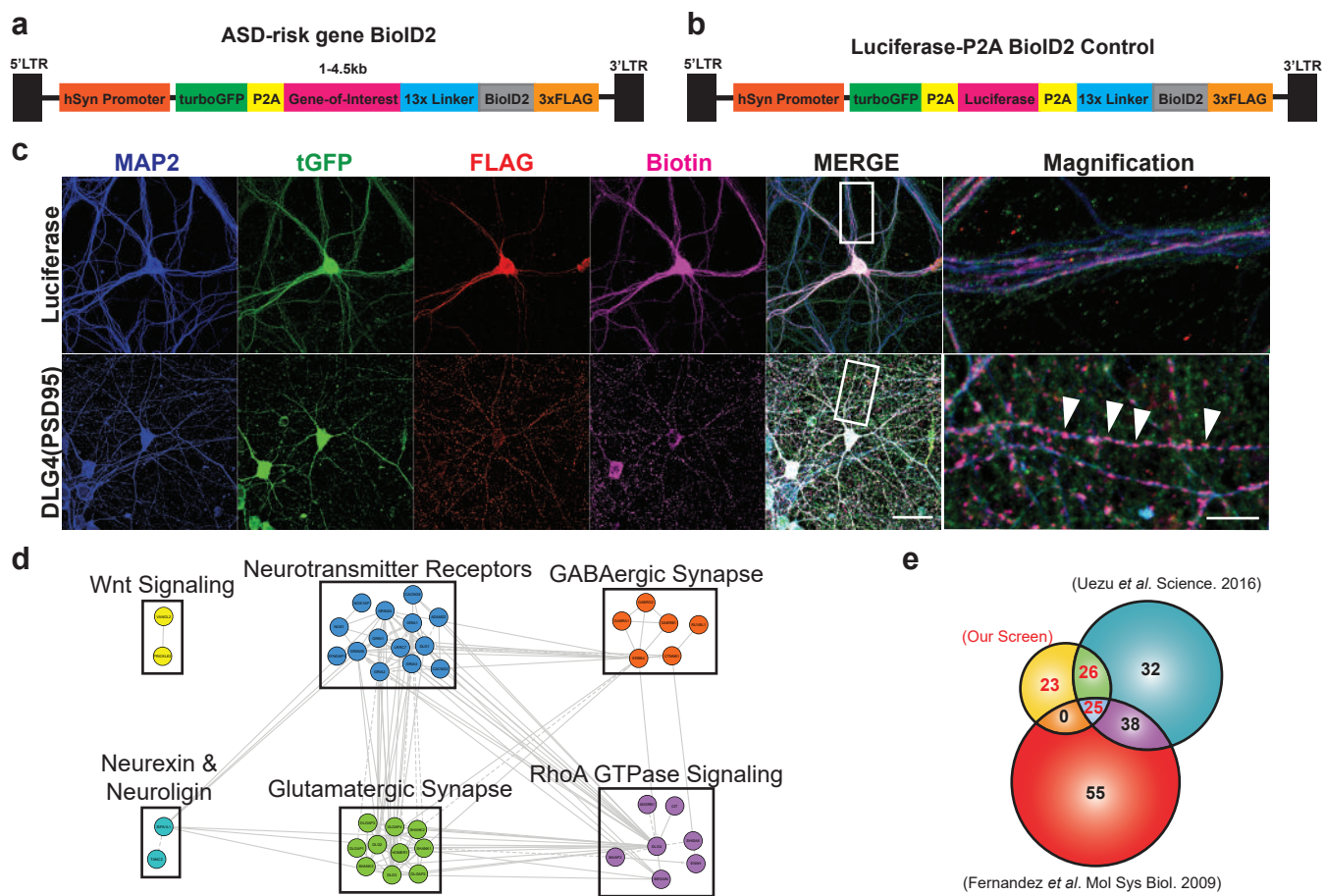


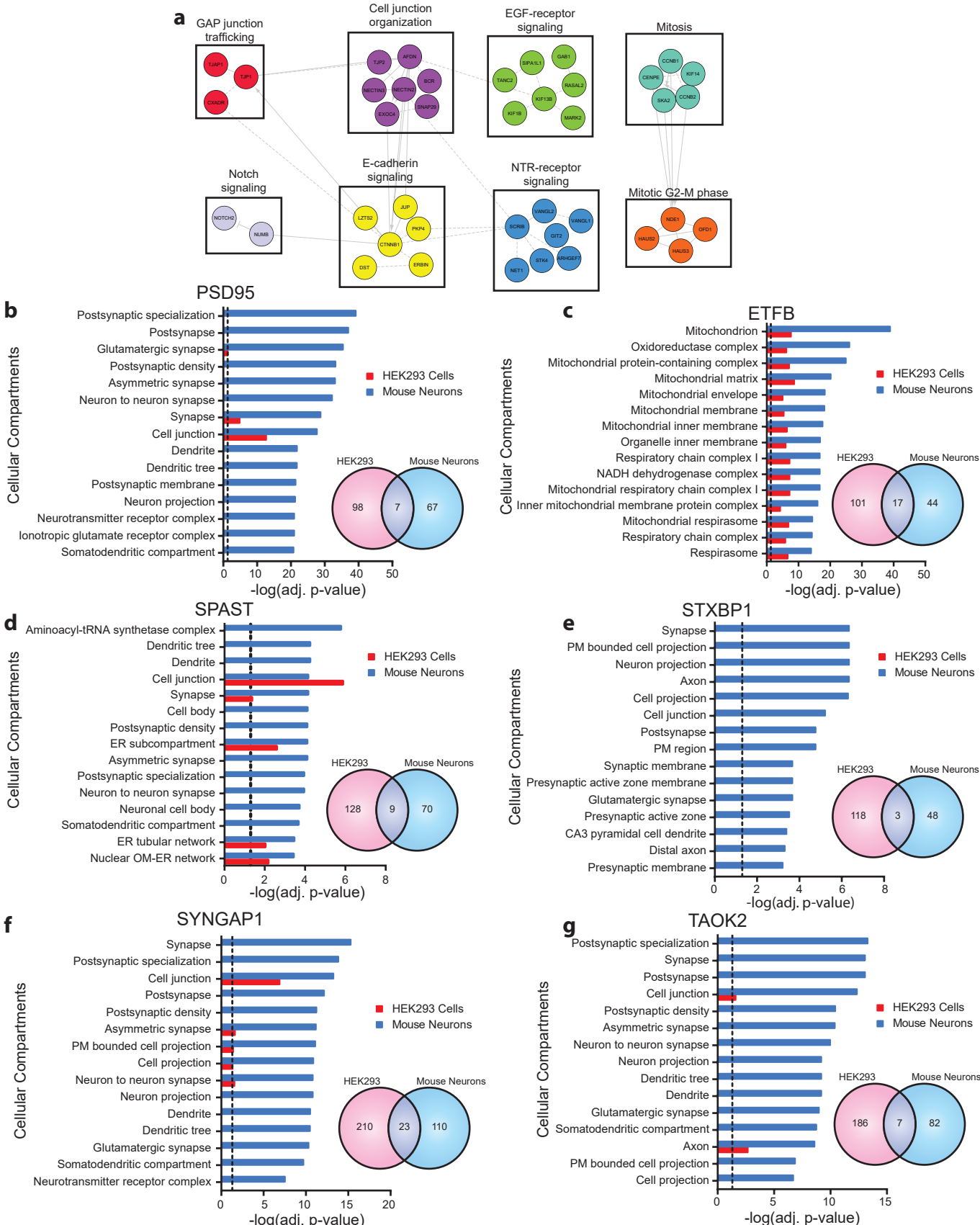
Figure 5. Shared ASD PPI network map network correlates to human brain development and disease pathology

a, Network of ASD-risk genes enriched in the shared ASD-risk gene PPI network. Large red nodes represent bait genes, while smaller colored nodes represent sharedness of ASD-risk genes between bait genes, between 1 (yellow) and 10 (blue) shared bait genes (g:Profiler, Benjamini-Hochberg FDR adj. $p < 0.05$). **b**, The shared ASD-risk gene PPI network enriches for human neuron cell types (Fisher's exact test). Dashed lines represent nominal ($p = 0.05$, left) and Bonferroni corrected ($p = 0.05/\text{number of cell types}$, right) significance thresholds. **c**, Enrichment of ASD differentially expressed genes (DEGs) in specific cell types. (Fisher's exact test). Dashed lines represent nominal ($p = 0.05$, left) and Bonferroni corrected ($p = 0.05/\text{number of cell types}$, right) significance thresholds. EN = excitatory neurons, IN = inhibitory neurons, RGC = radial glial cells, MGE RGC = medial ganglionic eminence, IPC = intermediate progenitor cells, Astro. = astrocyte, OPC = oligodendrocyte progenitor cells, Micro. = microglia, Endo. = endothelial cells, CP = choroid plexus cells, C-F = cortico-fugal, C-C = cortico-cortico, PV = parvalbumin, SST = somatostatin, VIP = vasoactive intestinal peptide, FB = fibrous, PP = protoplasmic, Neu_NRGN = neurogranin-expressing. Light blue bars have nominal p-value significance, while dark blue bars have Bonferroni corrected significance. **d**, Correlation plot of 41 ASD-risk genes through individual PPI networks. Genes were ordered by hierarchical clustering and clustered using kmeans ($k = 3$). **e**, Significant decrease in the average standard scores of individuals diagnosed with ASD, who have rare inherited missense mutations in Group 1 genes compared to Groups 2 and 3 (Non-parametric Kruskal-Wallis test, $p = 0.0103$, *post hoc* Dunn's test, Group 1 = 350, Group 2 = 113, and Group 3 = 416 probands). Box and whisker plot (minimum, 1st quartile, median, 3rd quartile, maximum).

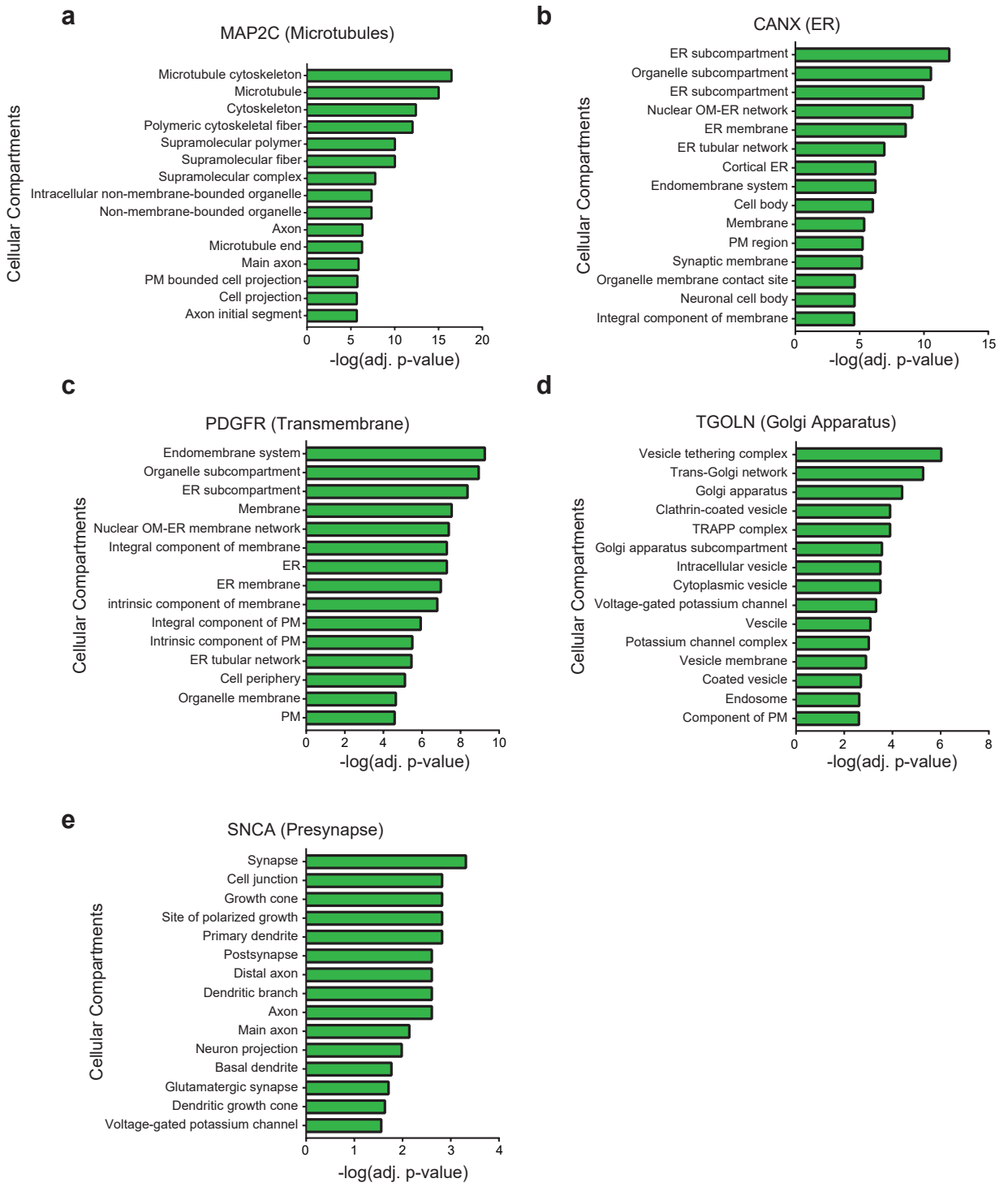


Extended Figure 1. BioID2 of DLG4 in mouse cortical neurons

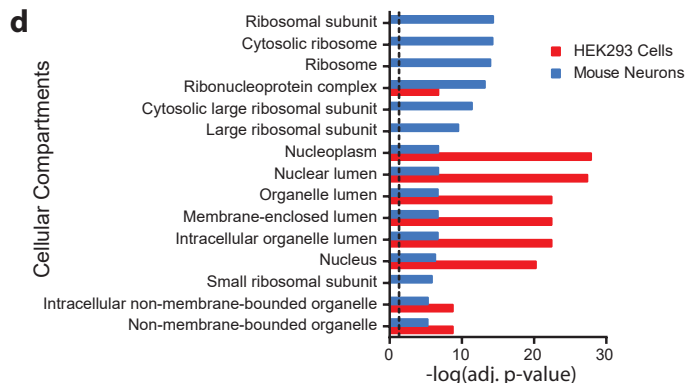
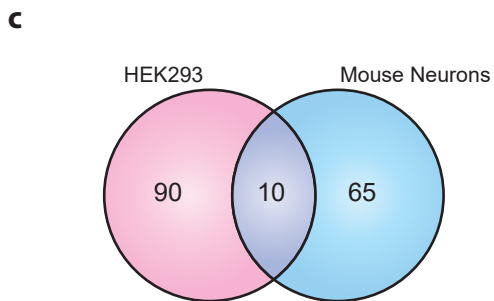
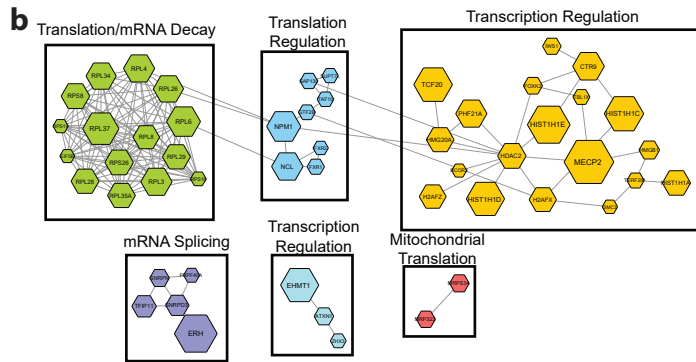
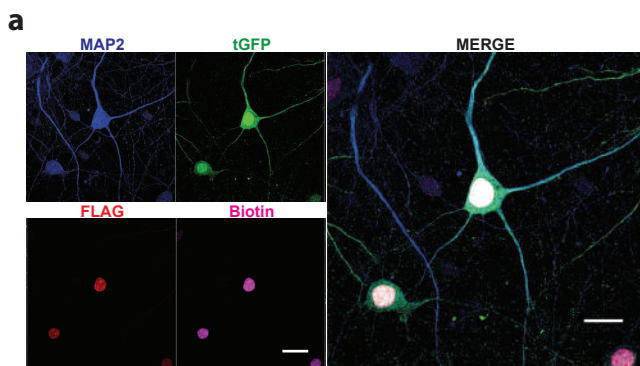
a, Diagram of the BioID2 fusion construct for the 41 ASD-risk genes. **b**, Diagram of the control Luciferase control fusion construct **c**, Representative images of cortical neurons infected with the PSD95-BioID2 and Luciferase-P2A-BioID2 constructs. Scale bar is 20µm. Magnified images are shown on the right. White arrows point to synaptic localization of PSD95-BioID2. Scale bar is 5µm. **d**, Reactome pathways enriched in the PSD95 PPI network. Clusters created using the Reactome FI app on Cytoscape and labeled with most significantly enriched pathways for each cluster (adj. $p < 0.05$). **e**, Venn diagram of shared protein interactors between our *in vitro* PSD95 PPI network and proteins identified by mouse *in vivo* PSD95 BioID (Uezu *et al.* 2016) or mouse *in vivo* tandem affinity purification of PSD95 (Fernandez *et al.* 2009).



Extended Figure 2. Comparison of ASD-risk gene PPI networks from BioID2 in HEK293 cells and mouse cortical neurons
a, Reactome pathways enriched in the PSD95 PPI network from HEK293 cells. Clusters created using the Reactome FI app on Cytoscape and labeled with the most significantly enriched pathways (adj. $p < 0.05$). **b-g**, Top 15 cellular compartments from mouse cortical neurons (blue) enriched in the PPI networks of PSD95, ETFB, SPAST, STXBP1, SYNGAP1, and TAOK2 compared to enrichment in HEK293 cells (red) (g:Profiler, Benjamini-Hochberg FDR adj. $p < 0.05$). Adjacent Venn diagrams show shared protein interactors identified by BioID2 in HEK293 cells vs mouse cortical neurons. PM: Plasma membrane, OR: Outer membrane, ER: endoplasmic reticulum.

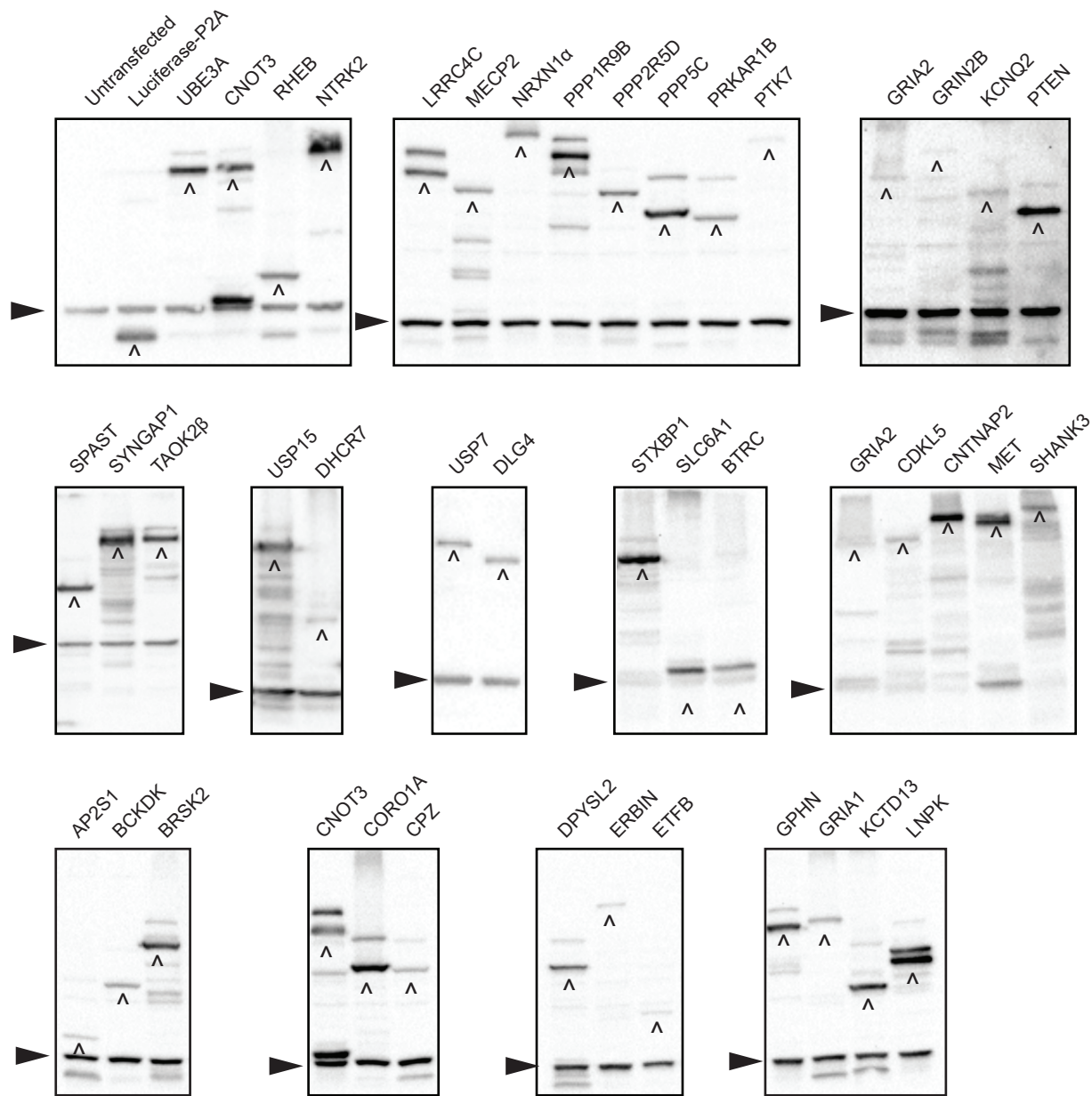


Extended Figure 3. Validation of BioID2 using genes localized to specific compartments in mouse cortical neurons
 BioID2 of cellular compartment proteins MAP2C (a), CANX (b), PDGFR (transmembrane domain) (c), TGOLN (d), and SNCA (e). g:Profiler pathway enrichment was used to identify significantly enriched cellular compartments (g:Profiler, Benjamini-Hochberg FDR adj. $p < 0.05$). PM: plasma membrane, OM: outer membrane, ER: endoplasmic reticulum.



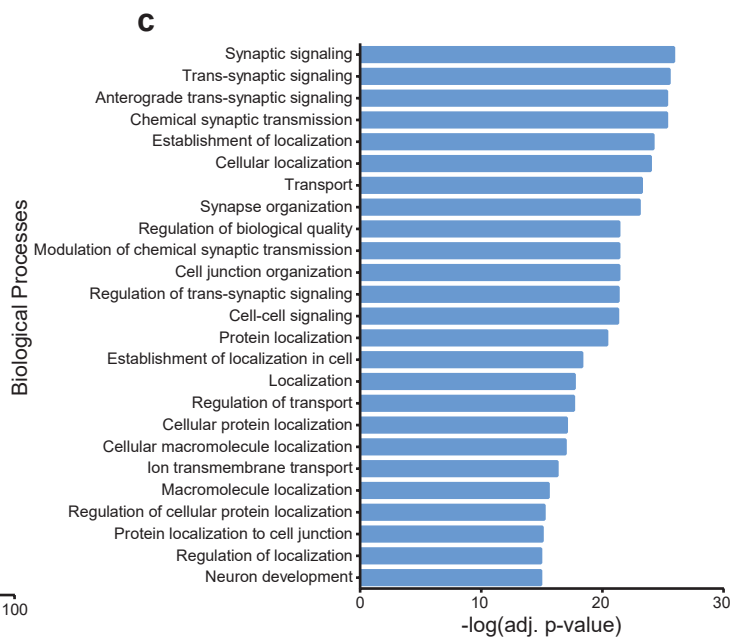
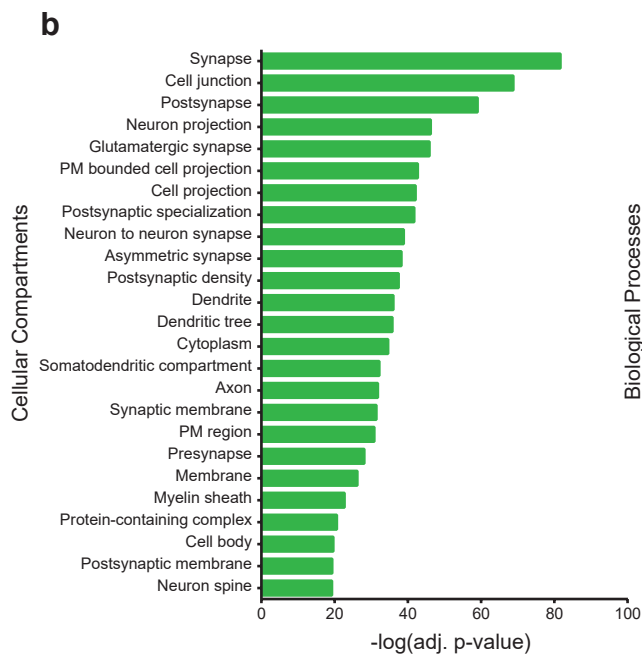
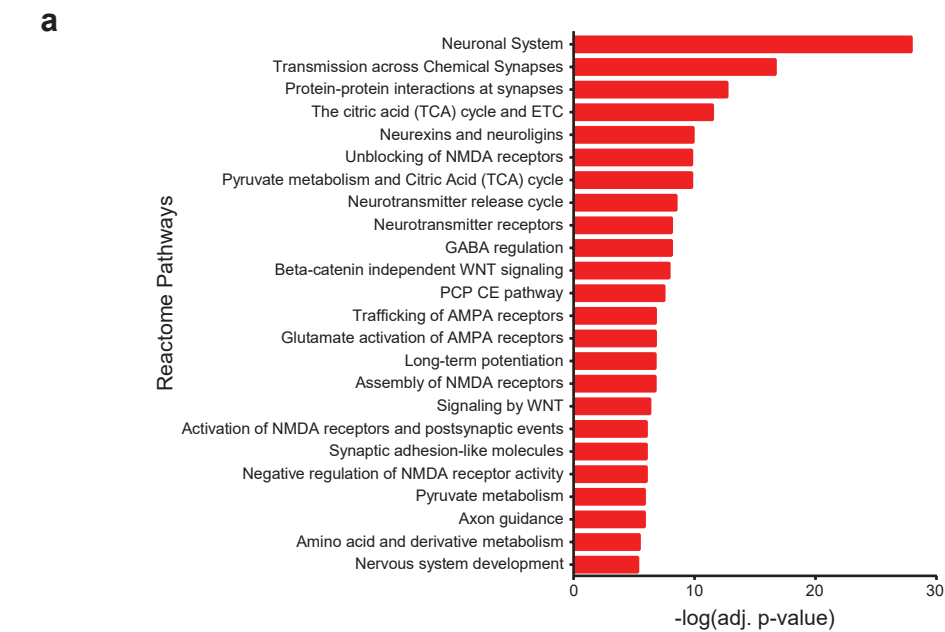
Extended Figure 4. BioID2 of MECP2 in mouse cortical neurons

a, Representative images of cortical neurons infected with the MECP2-BioID2 construct. Scale bar is 20 μ m. **b**, Reactome pathways enriched in the MECP2 PPI network. Clusters created using the Reactome FI app on Cytoscape and labeled with most significantly enriched pathways (adj. $p < 0.05$). **c**, Venn diagram shows shared protein interactors identified by BioID2 in HEK293 cells vs mouse cortical neurons. **d**, Top 15 cellular compartments from mouse cortical neurons (blue) enriched in the MECP2 PPI network compared to enrichment in HEK293 cells (red) (g:Profiler, Benjamini-Hochberg FDR adj. $p < 0.05$).



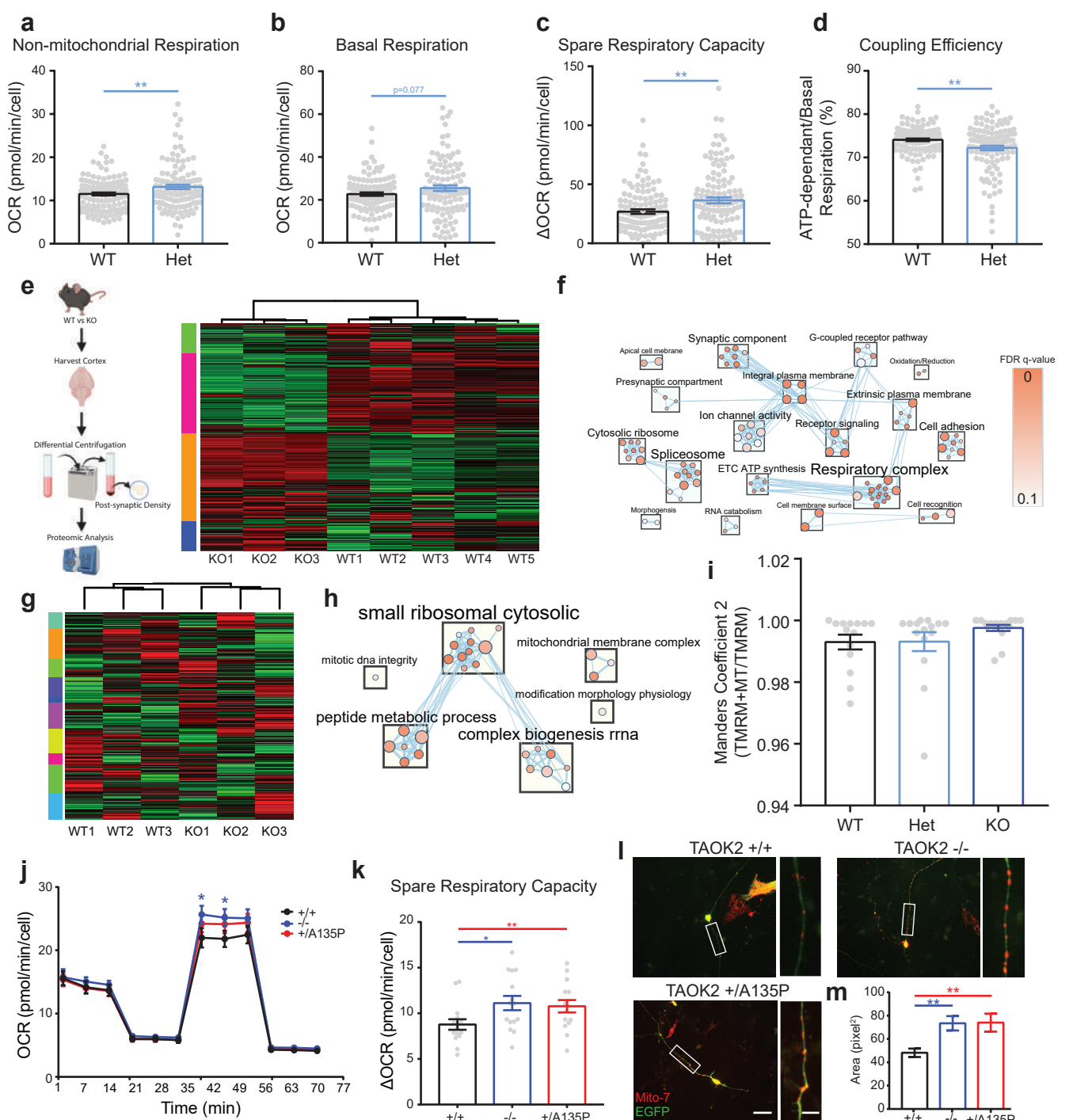
Extended Figure 5. Western blots of 41 ASD-risk gene Bioid2 constructs

Western blots of ASD-risk gene Bioid2 constructs transfected in HEK293 cells and immunoblotted for FLAG and β-actin as the loading control. ^ denotes expected Bioid2 fusion protein size. Bands higher than the caret indicated bands are possible tGFP fusion proteins due to P2A inefficiency. Arrow denotes β-actin loading control. Bands lower than β-actin are possible degraded Bioid2-FLAG proteins.



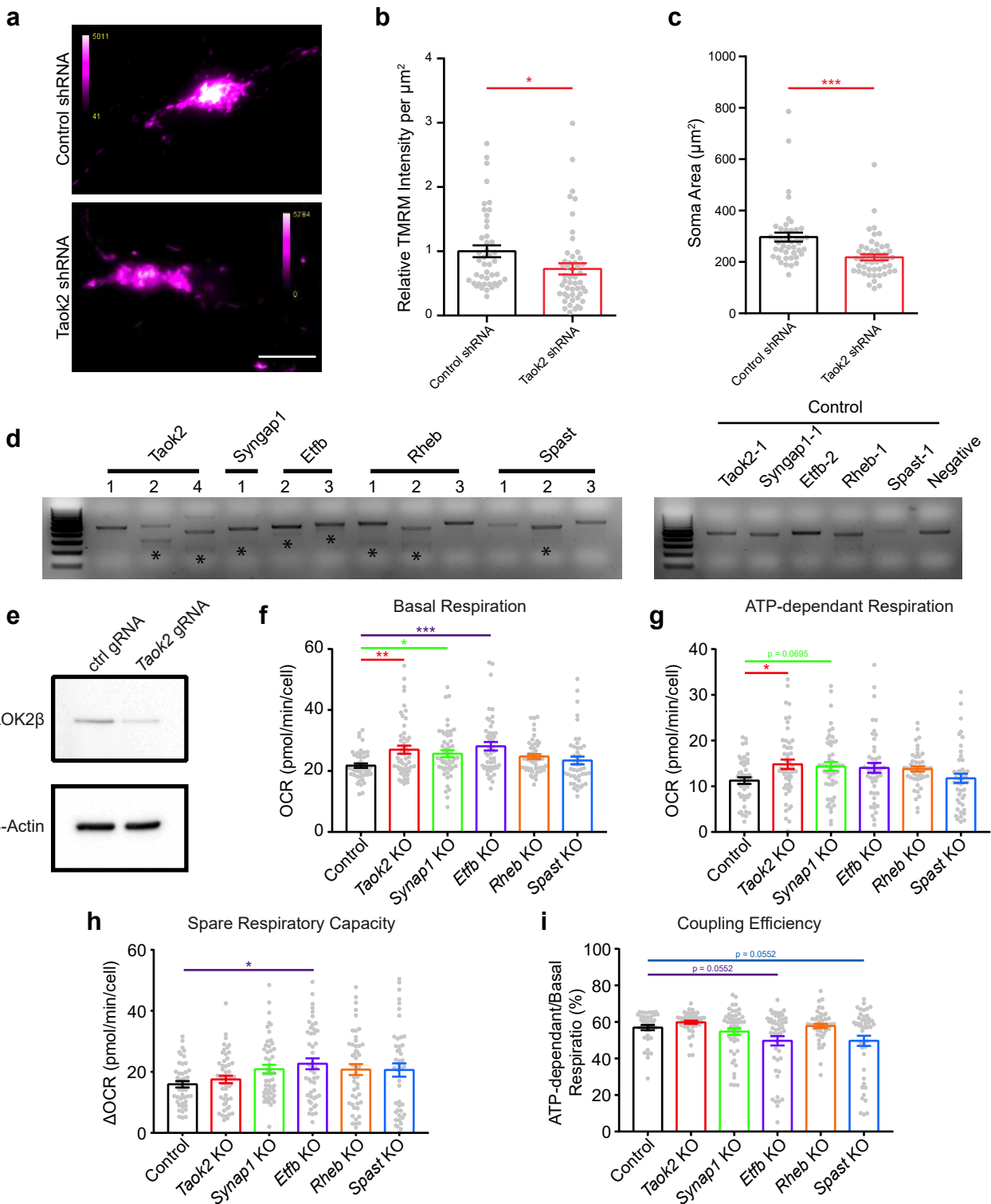
Extended Figure 6. Enriched pathways in the shared ASD-risk gene PPI network map identified using BioID2

Pathway enrichment was used to identify significantly enriched Reactome pathways (a), cellular compartments (b), and biological processes (c) (g:Profiler, Benjamini-Hochberg FDR adj. $p < 0.05$). The top 25 pathways are shown for each graph. PM: plasma membrane, OM: outer membrane, ER: endoplasmic reticulum.



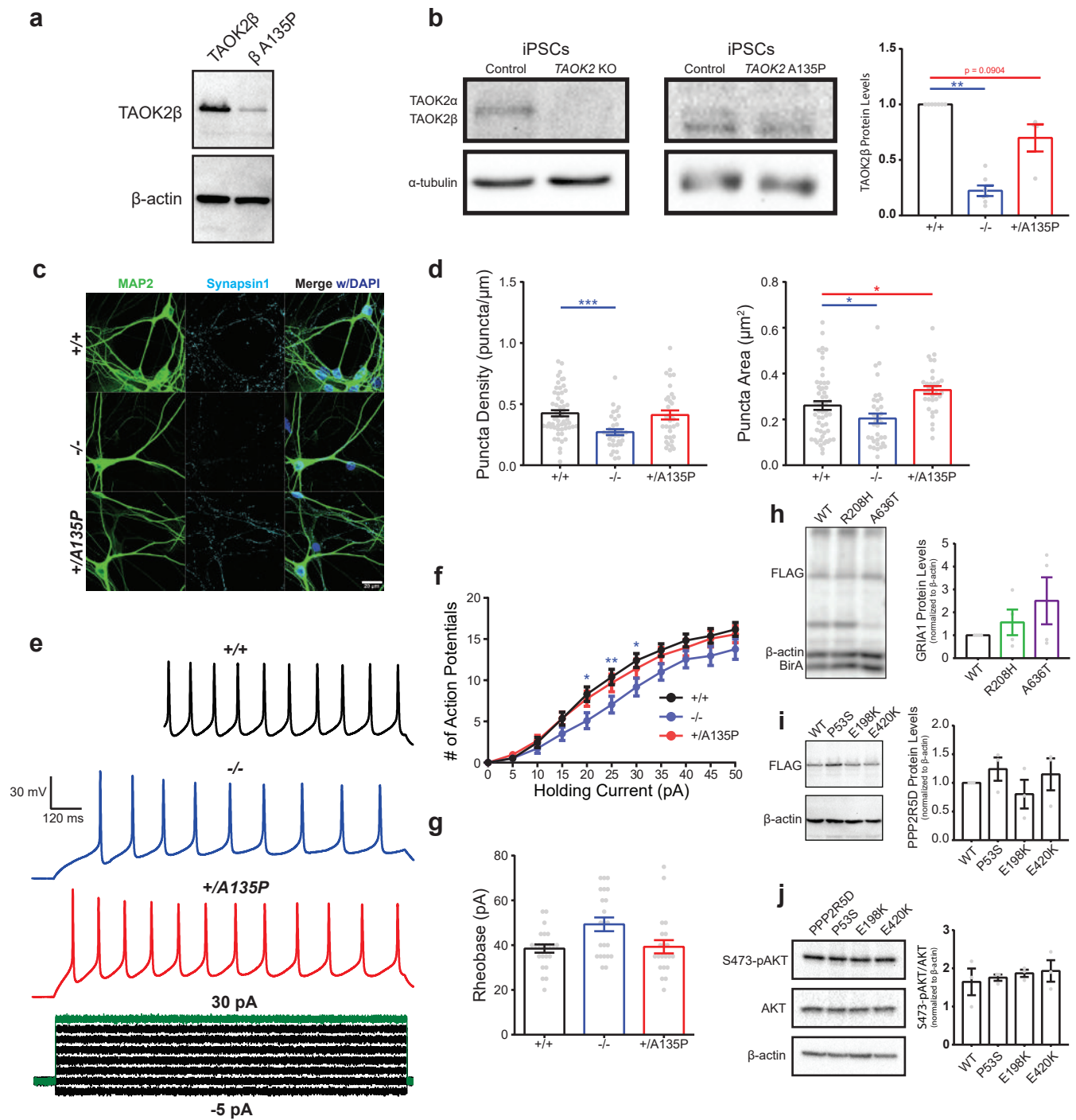
Extended Figure 7. Loss or disruption of *TAOK2* causes alterations in cellular respiration and mitochondrial proteins.

a-d, *Taok2* Het neurons have increased non-mitochondrial respiration and spare respiratory capacity, and decreased coupling efficiency (ROUT outlier test, $Q = 0.1\%$; Two-tailed unpaired t-test, non-mitochondrial respiration: $t = 2.668$, $df = 228$, $p = 0.0082$, basal respiration: $t = 1.776$, $df = 227$, $p = 0.0770$, spare respiratory capacity: $t = 3.007$, $df = 234$, $p = 0.0029$, coupling efficiency: $t = 3.146$, $df = 220$, $p = 0.0019$; WT = 118 wells, Het = 122 wells from three separate cultures). **e**, Shotgun proteomics of post-synaptic density fraction from *Taok2* WT and KO mouse cortices. **f**, *Taok2* KO PSD fractions have significant decrease in synaptic and mitochondrial protein gene sets (GSEA, $FDR < 0.1$; five *Taok2* WT and three *Taok2* KO mice littermates). Size of nodes represents number of proteins and color represents FDR q-value. **f**, RNA sequencing of *Taok2* WT and KO mouse cortices. **g-h**, *TAOK2* KO mouse cortices have altered mRNA levels of mitochondrial membrane proteins. (GSEA, $FDR < 0.1$, three *Taok2* WT and KO mice littermates each). Size of nodes represents number of proteins and color represents FDR q-value. **i**, All active mitochondria stained by MitoTracker (One-Way ANOVA, $F(2, 42) = 1.355$, $p = 0.2689$, *post hoc* Holm-Sidak test; WT = 14, Het = 15, KO = 15 neurons from three separate cultures). **j-k**, DIV7 *TAOK2* KO human neurons have significantly increased maximal respiration (Two-Way ANOVA, $F(2, 42) = 0.659$, $p = 0.5226$ between genotypes, *post hoc* Holm-Sidak test; WT = 118 wells and Het = 122 wells from three separate cultures). *TAOK2* KO and A135P neurons have significantly increased spare respiratory capacity (One-Way ANOVA, $F(2, 42) = 3.409$, $p = 0.0424$, *post hoc* Holm-Sidak test; WT = 118 wells, Het = 122 wells from three separate cultures). **l**, Representative images of human neurons transfected with Mito7-DsRed constructs at DIV7 and fixed and imaged at DIV9. Scale bar is 20 μm . Magnification of boxed areas shown on the right. Scale bar is 5 μm . **m**, *TAOK2* KO and A135P neurons have larger Mito7-DsRed punctae size compared to wildtype neurons (One-Way ANOVA, $F(2, 1309) = 5.032$, $p = 0.0067$, *post hoc* Holm-Sidak test; WT = 371, KO = 520, A135P = 421 punctae from 15-16 neurons per genotype). Mean \pm s.e.m. * $p < 0.05$, ** $p < 0.01$.

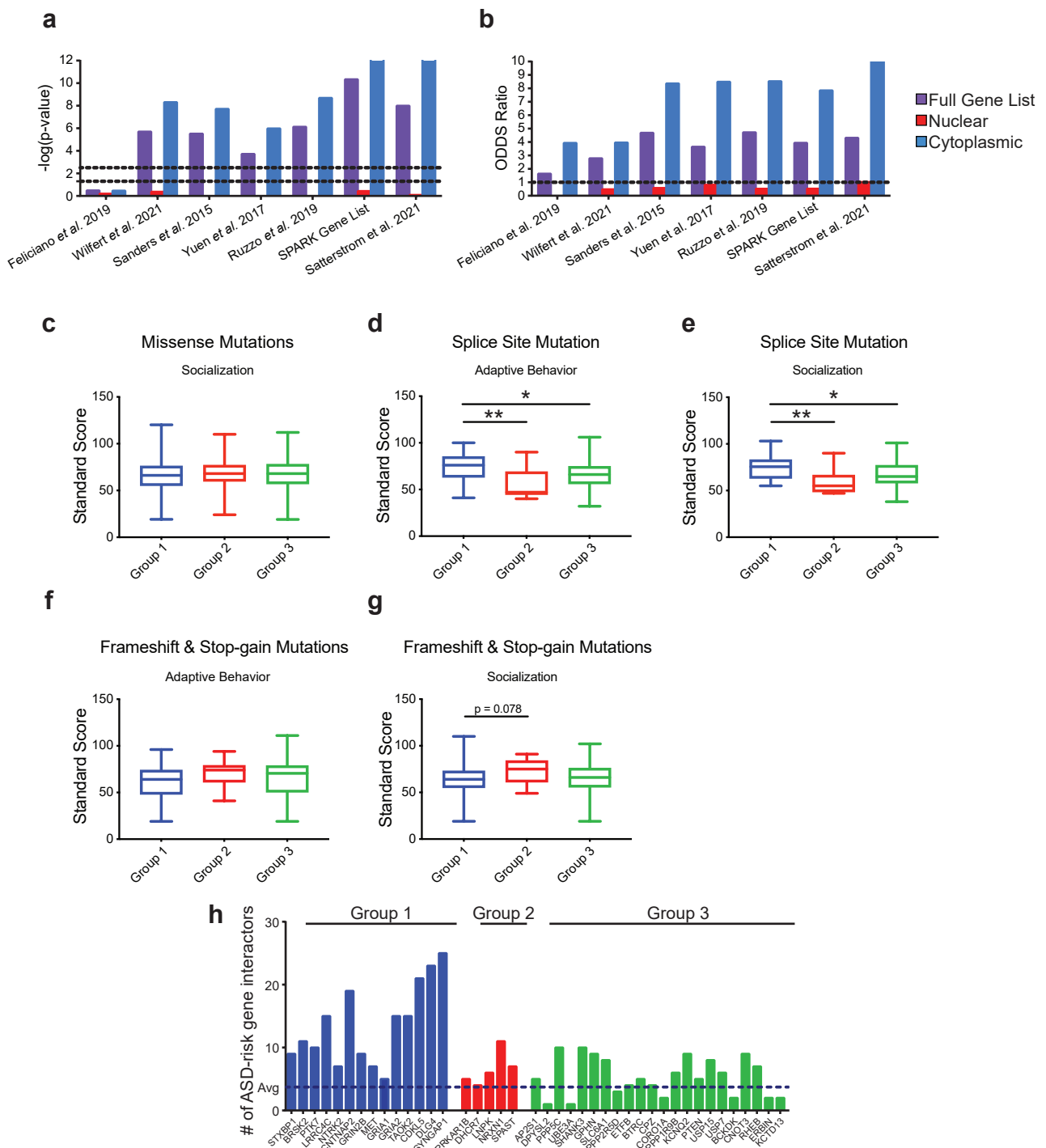


Extended Figure 8. Acute knockout of ASD-risk genes in mouse cortical neurons alters mitochondrial activity and cellular respiration

a, Representative images of mouse cortical neurons infected with control shRNA or *Taok2* shRNA showing TMRM intensity. Scale bar is 10 μm . **b**, Mouse cortical neurons with acute knockout of *Taok2* have decreased relative TMRM activity, even with decreased soma size (**c**) (TMRM activity: Unpaired t-test, $t = 2.156$, $df = 91$, $p = 0.0337$; WT = 44, *Taok2* KD = 49 neurons from two separate cultures). **d**, GeneArt cleavage assay kit shows indel insertion in at least 1 gRNA target region in mouse cortical neurons based on presence of multiple bands. *Indicates secondary band due to digested indel. **e**, Reduced *Taok2* protein expression in mouse cortical neurons infected with Cas9 and *Taok2* gRNAs. Infected at DIV7 and harvested at DIV18 for western blot of TAOK2 β . **f-i**, Significant changes in different aspects of cellular respiration (Basal respiration (**f**), ATP-dependent respiration (**g**), spare respiratory capacity (**h**), and coupling efficiency (**i**)) in mouse cortical neurons with CRISPR/Cas9 KO of *Taok2*, *Syngap1*, or *Etfb* (ROUT Outlier Test, $Q = 0.1\%$; basal respiration: One-Way ANOVA, $F(5,279) = 3.994$, $p = 0.0016$, ATP-dependent respiration: One-Way ANOVA, $F(5,279) = 2.517$, $p = 0.0300$, spare respiratory capacity: One-Way ANOVA, $F(5,276) = 2.381$, $p = 0.0389$, coupling efficiency: One-Way ANOVA, $F(5,263) = 4.894$, $p = 0.0003$, *post hoc* Holm-Sidak test; *Taok2* KO = 51 wells, *Syngap1* KO = 50 wells, *Etfb* KO = 47 wells, *Rheb* KO = 48 wells, *Spast* KO = 45 wells from five separate cultures). Mean \pm s.e.m. * $p < 0.05$, ** $p < 0.01$, *** $p < 0.001$.



Extended Figure 9. De novo mutations in TAOK2 caused altered synaptic transmission and neuron firing. **a**, Western blot of TAOK2 WT and A135P BioID2 constructs. **b**, Western blot of CRISPR/Cas9-edited iPSCs and neurons showing loss of TAOK2 expression in TAOK2 KO (-/-) and A135P (+/A135P) lines (One-sample t-test, WT vs KO: $t = 16$, $df = 6$, $p < 0.0001$, WT vs A135P: $t = 2.465$, $df = 3$, $p < 0.0904$; WT = 7, KO = 7, A135P = 4 wells from separate iPSC cultures). **c**, Representative images of TAOK2 WT (+/+), KO, and A135P human neurons, stained with MAP2, Synapsin 1, and DAPI 21 days after NG2 induction. **d**, Reduced synapsin puncta density and size in TAOK2 KO neurons (Left) and increased synapsin puncta size in TAOK2 A135P neurons (Right) (ROUT outlier test, $Q = 0.1\%$, One-Way ANOVA, density: $F(2, 120) = 8.104$, $p = 0.0005$, area: $F(2, 119) = 8.207$, $p = 0.0005$, post hoc Holm-Sidak test; WT = 55, KO = 35, A135P = 34 neurons from five separate transductions). **e**, Representative traces of repetitive firing (top) and current injection (bottom). **f**, TAOK2 KO neurons have reduced repetitive firing (Two-Way ANOVA, $F(2, 693) = 17.6$, $p < 0.0001$ between genotypes; WT = 23, KO = 22, A135P = 21 neurons from 3 separate transductions) increased rheobase (**g**) (One-Way ANOVA, $F(2, 63) = 5.229$, $p = 0.0079$; WT = 23, KO = 22, A135P = 21 neurons from 3 separate transductions). **h**, Representative western blot of GRIA1 WT, R208H, and A636T BioID2 constructs (left) and quantification (right) showing no significant difference (One-sample t-test, WT vs R208H: $t = 1.008$, $df = 3$, $p = 0.3877$, WT vs A636T: $t = 1.466$, $df = 3$, $p = 0.2388$; four separate transfections). **i**, Representative western blot of PPP2R5D WT, P53S, E198K, and E420K BioID2 constructs (left) and quantification (right) showing no difference in expression (One-sample t-test, WT vs P53S: $t = 1.185$, $df = 2$, $p = 0.3577$, WT vs E198K: $t = 0.7838$, $df = 2$, $p = 0.5152$, WT vs E420K: $t = 0.5371$, $df = 2$, $p = 0.6449$; three separate transfections). **j**, Representative western blot of p-AKT and AKT in HEK293 cells expressing PPP2R5D WT or variant constructs (left) and quantification (right) showing no difference in the pAKT/AKT ratio (One-way ANOVA, $F(3, 8) = 0.2948$, $p = 0.8283$; three separate transfections). Mean \pm s.e.m. * $p < 0.05$, ** $p < 0.01$, *** $p < 0.001$.



Extended Figure 10. Enrichment of ASD risk-genes in the shared ASD PPI network map and grouping of clinical phenotypes

a, Enrichment of full gene list, cytoplasmic gene only lists, and nuclear gene only lists from published works and SPARK, in the shared ASD-risk gene PPI network shown by significance. (Fisher's exact test). Dashed lines represent nominal ($p = 0.05$, left) and Bonferroni corrected ($p = 0.05/\text{number of cell types}$, right) significance thresholds. **b**, ODDS ratio of full gene list, cytoplasmic gene only lists, and nuclear gene only lists enriched in the shared ASD-risk gene PPI network. **c**, Individuals with missense mutations in Cluster 1, 2 and 3 genes show no significant differences in socialization standard scores (Non-parametric Kruskal-Wallis test, $p = 0.1765$, *post-hoc* Dunn's test; Group 1 = 351, Group 2 = 114, and Group 3 = 416 probands). **d-e**, Individuals with splice site mutations in Cluster 1 have significantly higher adaptive behavior and socialization standard scores than Cluster 2 and 3 (Non-parametric Kruskal-Wallis test, adaptive behaviour: $p = 0.0036$, Group 1 = 32, Group 2 = 9, and Group 3 = 72 probands; socialization: $p = 0.0021$, Group 1 = 32, Group 2 = 9, and Group 3 = 71 probands; *post hoc* Dunn's test). **f-g**, Individuals with frameshift or stop gain mutations in Cluster 1, 2 and 3 genes show no significant differences in adaptive behavior and socialization standard scores (Non-parametric Kruskal-Wallis test, adaptive behaviour: $p = 0.1069$, Group 1 = 51, Group 2 = 19, and Group 3 = 60 probands; socialization: $p = 0.0803$, Group 1 = 51, Group 2 = 19, and Group 3 = 60 probands; *post hoc* Dunn's test). **h**, Number of ASD-risk genes identified in each of the 41 ASD-risk gene protein-protein interactions. Dashed line represents average expected risk genes. Box and whisker plot (minimum, 1st quartile, median, 3rd quartile, maximum). * $p < 0.05$, ** $p < 0.01$.

Table S1. BioID2 PPI networks of 41 ASD-risk genes and cellular compartment genes

Table S2. Comparison of BioID2 PPI networks identified in HEK293 cells and mouse cortical neurons

Table S3. Comparison of BioID2 PPI network enriched cellular components identified in HEK293 cells and mouse cortical neurons

Table S4. BioID2 PPI network enriched cellular components of compartment specific genes

Table S5. BioID2 PPI network enriched pathways of 41 ASD-risk genes

Table S6. 41 ASD-risk gene PPI network map enriched pathways

Table S7. Differentially expressed genes and proteins and dysregulated pathways in *Taok2* KO mouse cortices

Table S8. Comparison of BioID2 PPI networks between ASD-risk genes and their variants

Table S9. BioID2 PPI network enriched pathways of ASD-risk genes and their variants

Table S10. List of sources for 41 ASD-risk genes and cellular compartment genes

Table S1-S10 are posted online as Excel Files